Setup of a Goniometer System for the Production of Linearly Polarised Photons for the BGO-OD Experiment at ELSA

Diplomarbeit in Physik
von
Andreas Bella

angefertigt im
Physikalischen Institut,
vorgelegt der
Mathematisch-Naturwissenschaftlichen Fakultät
der
Rheinischen Friedrich-Wilhelms Universität Bonn

im März 2011

Eidesstattliche Erklärung

Eidesstattliche Erklärung zur Diplomarbeit

Ich versichere, die von mir vorgelegte Arbeit selbstständig verfasst zu haben. Alle Stellen, die wörtlich oder sinngemäß aus veröffentlichten oder nicht veröffentlichten Arbeiten anderer entnommen sind, habe ich als entnommen kenntlich gemacht. Sämtliche Quellen und Hilfsmittel, die ich für die Arbeit benutzt habe, sind angegeben. Die Arbeit hat mit gleichem Inhalt bzw. in wesentlichen Teilen noch keiner anderen Prüfungsbehörde vorgelegen.

$Unterschrift$: $Ort, Datum$:

Autor: Andreas Bella

Referent Prof. Dr. Hartmut Schmieden
Koreferent Prof. Dr. Jochen Dingfelder

"I am only a child playing on the beach,
while vast oceans of truth lie undiscovered before me."
Sir Isaac Newton (1643-1727)

Contents

List of Figures

List of Tables

1 Introduction

For a long time, the atom was considered as indivisible. In 1897, Thomson discovered the electron, while studying cathode rays of different materials. This find disproved the concept of the indivisible atom. In 1909 Rutherford, Geiger and Marsden dicovered with their scattering experiments that the atom had to consist of a pointlike charged nucleus, which concentrates the overwhelming fraction of the atom. Ten years later, Rutherford found the proton as a constituent of the atomic nucleus, by irradiating nitrogen with α-particles. It took another thirteen years, when Chadwick discovered the neutron by irridiating beryllium with α-particles. Rutherford had postulated the neutron already in 1921, because he was of the opinion that a neutral particle is needed to compensate the repelling Coulomb force due to the charge of the proton and therefore to prevent the nucleus breaking apart. In 1968, deep elastic scattering experiments at the Stanford Linear Accelerator Center (SLAC) also showed that nucleous are not elementary particles. They consist of pointlike particles, which are known as quarks.

Today, six different types of quarks (*up*, *down*, *charm*, *strange*, *top*, *bottom*) and their antiparticles are known. Particles, which are composed of quarks, are called hadrons and classified into baryons and mesons. While Baryons, like the proton and the neutron, are composed of three quarks or antiquarks, mesons consists of a quark and a antiquark. All quarks come in three different colours (*red*, *blue*, *green*) and their anticolours. These colours are the charges of the strong interaction, which is responsible for the cohesion of the quarks.

A particular feature of these quarks is, that a system consisting of quarks has to be of neutral colour. It is not possible to detect them as free particles. This effect can be described by a strong coupling constant, which depends strongly on the distance between the quarks and therefore on the transferred momentum $\alpha_s(Q^2) \sim \frac{1}{ln(Q^2)}$. The consequences are that, for low distances, quarks can be seen as quasi-free particles ($asymptotic\ freedom$), while at large distances, the coupling increases so strong, that is not possible to seperate these quarks from each other.

If more energy is spent in seperating these quarks from each other, at a certain threshold, a quark antiquark pair will be produced (*confinement*).

In contrast to the atom, it is not possible to describe the excitation spectra of hadrons within perturbation theory. Various models have been developed, which are based on investigations of the hadron's excitation spectra. With these models it is possible to describe a lot of excitation resonances, but there are also deviations, which leave open questions. Amongst others, the quark models predict a larger amount of excited resonances, as observed before. To study these deviations from the quark models, photoproduction experiments are well suited, where high energy photons with $E_\gamma \sim 3\,\mathrm{GeV}$, are used to excite nuclei. The excited resonances decay nearly instantly into mesons, which decay further into lighter mesons or photons. By investigating these final decay states, it is possible to reconstruct the excited resonances within a theoretical framework.

The Crystal Barrel (CB) experiment at the University of Bonn, is specialised to find states involving neutral mesons. For the detection of charged mesons, the BGO-OD[1] experiment, which is currently set up and described in the next chapter, is complementary. It efficently detects both, charged and neutral, reaction products. Both experiments require a photon beam of known energy. In order to realise this by electron bremsstrahlung, the method of *photon tagging* is used, which is described in chapter 3. Additional information about the nucleon spectrum can be achieved by using polarisation degrees of freedom. For this purpose linearly or circularly polarisation photon beams are an essential tool. Taking advantage of the effect of coherent bremsstrahlung from a crystal lattice, it is possible to produce linearly polarised photons. The goniometer system which, as a part of the *tagging* system, is used to accurately position the crystal relative to the beam will be discussed in chapter 4. The process of incoherent and coherent bremsstrahlung, which is based on the theorie of H.A.Bethe [Bet34] and U.Timm [Tim69], is used for the determination of the degree of polarisation and introduced in chapter 5. Experimental effects, like the collimation of the photon beam, primary electron beam divergence and multiple scattering change the form of the intenisty spectra and must be considered in the calculations. The respective methods are presented in chapter 6. For the quantitative computation of coherent and incoherent bremsstrahlung intensity spectra a program code called COBRIS[2] was established within this thesis work

[1] The first part of the abbreviation denotes bismuth germanate, which is used for the crystals in the BGO-ball and the second part for the open dipole in the forward spectrometer

[2] Calculation of bremsstrahlung intensity spectra

and is explained in chapter 7. Measured data from the CB experiment is used to test the computation done by COBRIS. The results of the comparisions are presented in chapter 8. Finally a summary will be given in chapter 9.

2 The BGO-OD Experiment at ELSA

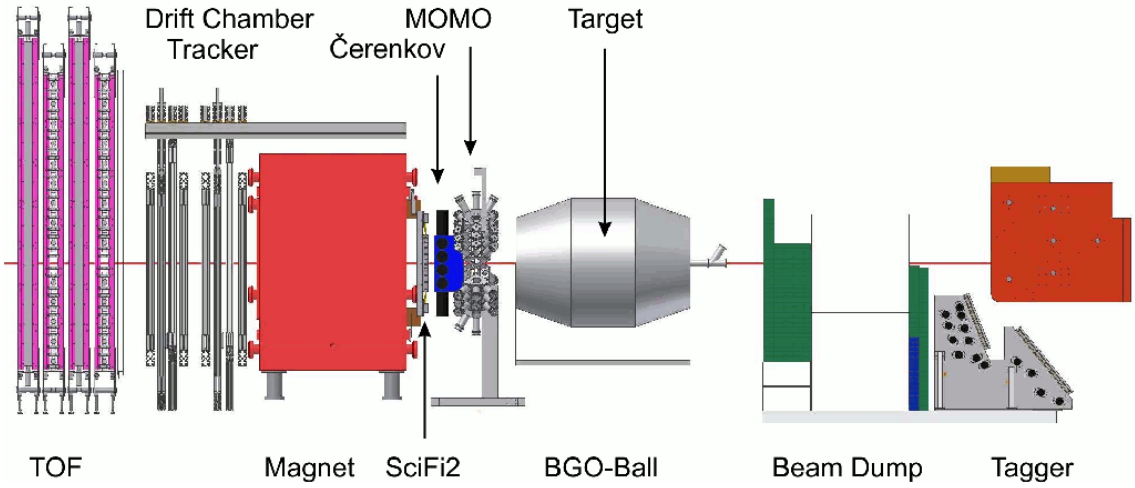

Figure 2.1: Overview of the BGO-OD experiment. The electron beam (from ELSA) enters from the right side. The tagging detector belongs to the old SAPHIR experiment [Wa] and will be replaced[Sie10]

The BGO-OD experiment will be used for systematic investigation of the photoproduction of mesons off the nucleon. One goal of the experiment is the investigation of the production mechanism in meson photoproduction and the formation of particular baryonic resonances. The complete setup is shown in figure 2.1 in which the beam comes from the right. High energy bremsstrahlung photons are used to excite the nucleons within the target. A real photon beam is produced from electrons impinging on a thin metal radiator. Unpolarised electrons produced with a thermal electron source and accelerated by the LINAC1[1] or LINAC2 of ELSA[2] reach the booster synchrotron with an energy of 20 MeV or 26 MeV, where they get accelerated up to an energy of 1,6 GeV. The electrons can be accelerated to a

[1] **L**inear **A**ccelerater
[2] **E**lectron **S**trecher **A**ccelerator

maximum energy of 3,5 GeV in the strecher ring, from where they can be extracted into the experimental area by slow resonant extraction. An overview of ELSA is shown in figure 2.2. After extraction into the experimental area, a quasi contin-

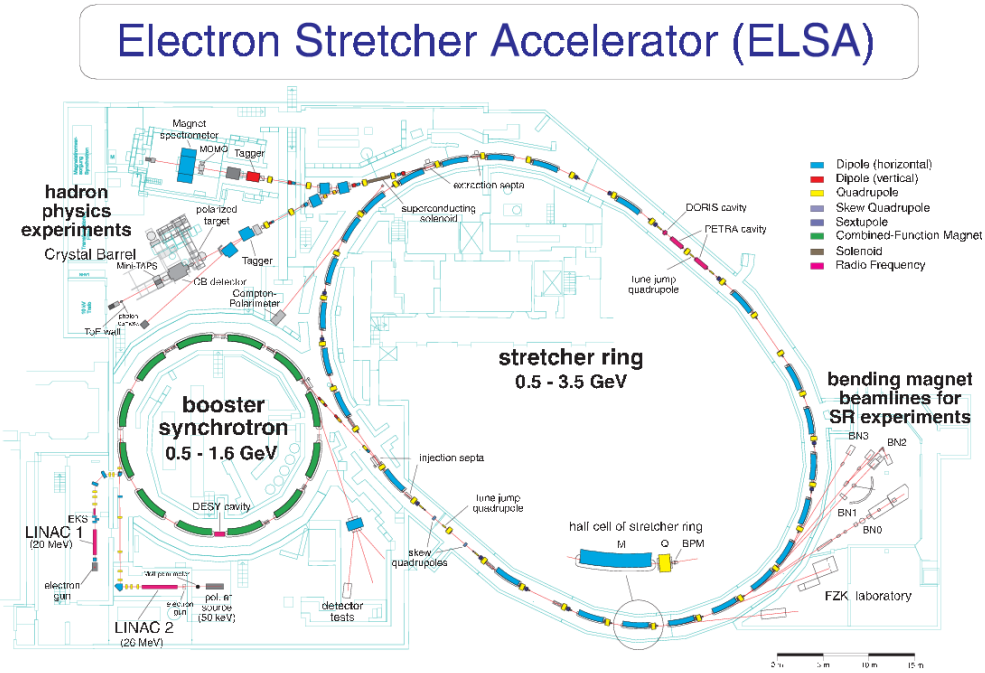

Figure 2.2: Overview of the Electron Stretcher Accelerator (ELSA) [ELSA]

ious electron beam enters the tagging system which consists of the goniometer, the tagging magnet and the hodoscope. By hitting a radiator, which is aligned by the goniometer, bremsstrahlung is generated due to the deflection of the electrons in the electromagnetic field of the atoms. By bending the trajectories of the electrons in the dipole magnet, the energy of the photons can be determined from the electron's radius of curvature. A more detailed description of the tagging system will be given in the next chapter. The produced photon beam reaches the center of the central detector setup and interacts with a liquid hydrogen or deuterium target, which remains in the center of the central detector, the BGO-OD ball. The decay products are detected in a detector setup, which covers nearly the 4π solid angle. It consists of the central detector and a forward magnetic spectrometer. The central detector, which is able to detect charged and uncharged particles consists of 480 bismuth germanate ($Bi_4Ge_3O_{12}$) crystals. For the identification of the particles emitted at extreme forward directions, and the reconstruction of their tracks, the forward magnetic spectrometer is used. It consists of two scintillating fiber tracking

detectors consisting of Scifi2[3] [Bös11] and MOMO[4] detector [Joo96] in front of the spectrometer magnet and eight drift chambers [Ham08], [Sch10] and four time of flight detectors [Ram07] behind the magnet.

[3] **S**ilicon **Fi**bres
[4] **M**onitor **o**f **M**esonic **O**bservables

3 Production of Polarised High Energy Photons

As mentioned before, high energy photons with energies in the order of $E_\gamma \sim 1\,\mathrm{GeV}$ can be used for the excitation of nucleon resonances. Two different methods are mainly used for the production of such photon beams. Laser backscattering and bremsstrahlung of high energy electrons. These two principles differ in their characteristics, like maximum photon energy, achievable photon flux and achievable polarisation of the photon beam. Table 3.1 provides an overview of different experiments, which use these two methods for the production of high energy photons and lists their characteristics. In the process of laser backscattering, laser light is scattered on highly energetic electron beam, whereas in the bremsstralung process accelerated electrons are deflected in the electromagnetic field of a thin radiator. In both cases, it is possible to determine the time of production and the energy of the produced photons by analysing the momentum of the scattered electrons. This method is called *photon tagging*.

The principle of laser backscattering and bremsstrahlung will be introduced in this chapter, followed by the presentation of the *photon tagging* method, which will be discussed in more detail for the case of bremsstrahlung.

Experiment	Method	$E_{\gamma,max}$ (GeV)	N_γ ($\mathrm{s}^{-1}\mathrm{MeV}^{-1}$)	$E_\gamma/E_{\gamma,max}$ (%)	$P^{lin}_{\gamma,max}$ (%)
CLAS [FP09]	Brems.	6	10^4	20-95	80@2 GeV
CB [Cre09]	Brems.	3.2	10^4	9-91	40@1.4 GeV
LEPS [LEPS]	Laser B.s.	2.4	10^3	60 - 100	98
GRAAL [Boc97]	Laser B.s.	1.7	10^3	33 -100	98
A2 [MGe08]	Brems.	1.5	10^5	5-93	50@0.8 GeV

Table 3.1: Properties of different production methods for highly energetic photon beams

3.1 Compton Backscattering

One possibility to produce highly energetic photon beams is by taking advantage of Compton scattering. An monoenergetic accelerated electron beam, which is produced for example in a storage ring [Boc97], is irradiated with laser light at an angle of almost 180°. The energy change is given by

$$E_\gamma^{sca} = E_\gamma^{laser} \frac{1 - \beta \cos\theta_1}{1 - \beta \cos\theta + (E_\gamma^{laser}/E_0)(1 - \theta_2))} \tag{3.1}$$

where β is the electron velocity in units of speed of light. While θ_2 and θ denote the angles of the scattered photon beam with respect to the incoming photon and the electron beam, and θ_1 indicates the angle between the incident photon and the electron beam. The kinematics is depicted is shown in figure 2.1. In the case of

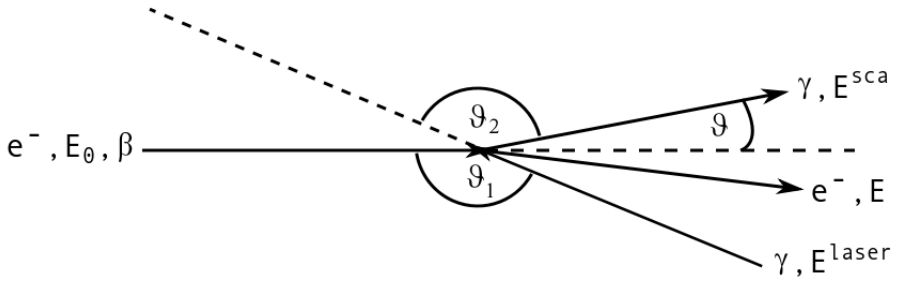

Figure 3.1: Kinematic description of the Compton laser backscattering process

relativistic electrons $\beta \approx 1$, $\theta_1 \approx \theta_2 \approx 180°$ and $\theta \ll 1$, equation 3.1 can be reduced as

$$E_\gamma^{sca} = \frac{4E_0 E_\gamma^{laser}}{1 + 4E_0 E_\gamma^{laser} + (E_0\theta)^2} \tag{3.2}$$

For the tagging of the photon two methods can be used which are called internal and external tagging. In the first case, the scattered electrons get deflected in the magnet of the storage ring which is used as a momentum analyser. By measuring the horizontal displacment of the scattered electrons from the main orbit in the ring, it is possible to determine the energy of the scattered photon. For external tagging, the scattered electrons are removed from the storage ring and momentum analysed in an external spectrometer, similar to the bremsstrahlung tagging which is decribed in the next section.

The method of laser backscattering with internal photon tagging was used in the GRAAL[1] experiment at the ESRF[2]. Accelerated electrons with energies of about 6 GeV were irradiated with laser light, produced by an Argon laser with wavelengths of 351 nm and 514 nm. The maximum photon energy of 1,5 Gev is achived in the scattering process. The electrons, which were scattered are seperated by the bending magnet from the unscattered electron beam with a distance of 56 mm and deflected into the tagging detector. The tagging detector is placed directly at the end of a bending magnet with a minimum distance of 14 mm to the unscattered electron beam. Typical photon rates which were achieved are about $N\gamma = 10^3 s^{-1} MeV^{-1}$. An overview is given in figure 3.2.

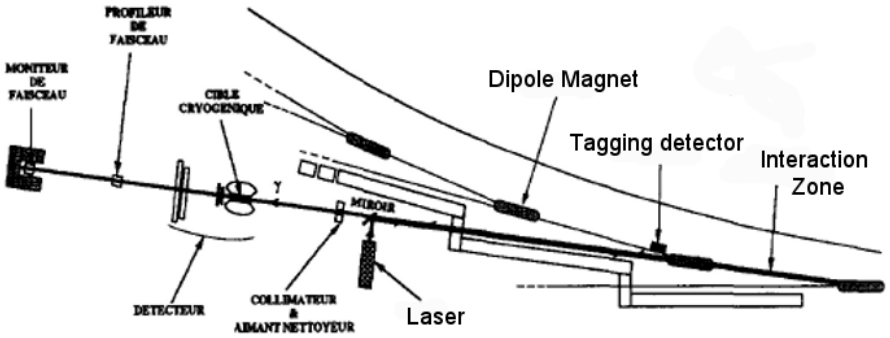

Figure 3.2: Illustration of the tagging system at GRAAL [Boc97]

3.2 Process of Bremsstrahlung

In the process of bremsstrahlung, monoenergetic accelerated electrons impinge on a thin ($\sim 100\,\mu$m) radiator, e.g. copper or nickel foil or a crystal lattice (s. chapter 5). By deflecting the electrons in the electromagnetic field of the atoms in the radiator, photons are radiated and emitted in the forward direction. To produce linear polarised photons by the process of coherent bremsstrahlung a crystal, e.g. diamond, instead of an amorphous radiator has to be used. The process of coherent bremsstrahlung is explained in chapter 5.2. Because the degree of polarisation and the energy range depends strongly on the orientation of the crystal with respect to the electron beam, the diamond crystal has to be aligned precisely. The maximum degree of polarisation, which can be achived at CLAS is

[1] **Gr**enoble **A**nneau **A**ccèlèrateur **L**aser
[2] **E**uropean **S**ynchrotron **R**adiation **F**acility

about 80% at $E_{gamma} = 2\,\mathrm{GeV}$. The big advantage of producing high energy photons by the process of bremsstrahlung is the higher photon production rate. With $N_\gamma \approx 10^5\,\mathrm{s}^{-1}\,\mathrm{MeV}^{-1}$ [MGe08], it is two orders of magnitudes larger than laser backscattering.

The general setup of a bremsstrahlung tagging system is shown in figure 3.3. It consists of the goniometer system, a dipole magnet and the tagging hodoscope. The primary electron beam enters from the left and is incidents upon the radiator.

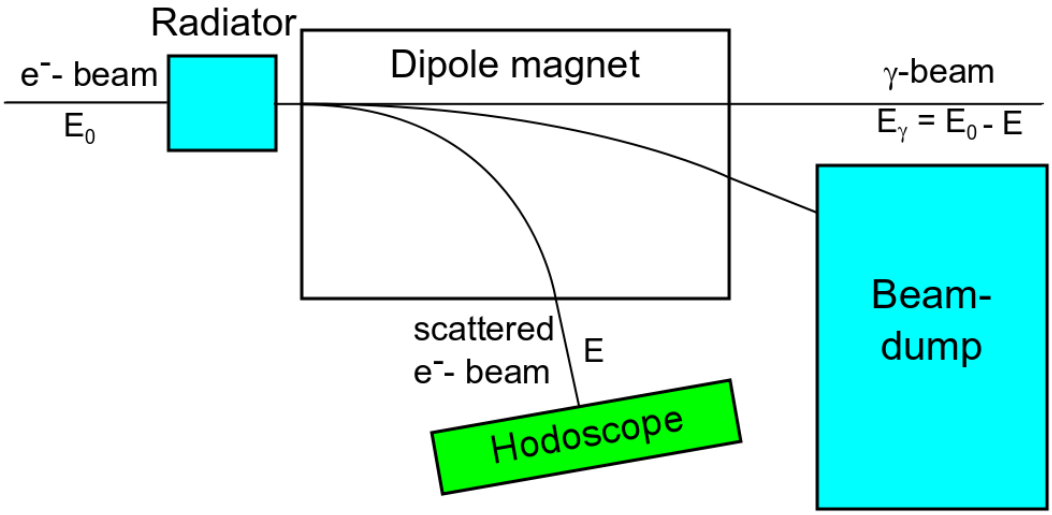

Figure 3.3: Principle of bremsstrahlung photon tagging

Electrons which are involved in the bremsstrahlung process lose a certain amount of their energy and are bent according to its momentum $p_e = e \cdot B \cdot r$ by the tagging magnet into the hodoscope, while the primary electrons are bent into a beam dump which does not belong directly to the tagging system but is needed to stop the primary beam. Measurements of the electron's radius of curvature, by detecting the impact point of the electrons in the hodoscope, allows the determination of their energy $E_{el,sca}$. Finally, for single scattering processes, the energy of the photon is given by $E_\gamma = E_{el,0} - E_{el,sca}$.

For the BGO-OD experiment, the process of bremsstrahlung will be used for the production of high energy photons. In the next section a short summary of the actual status of the tagging system will be given.

3.3 Bremsstrahlung Tagging at the BGO-OD Experiment

The tagging magnet for the BGO-OD experiment is identical to the magnet used in the neighboring Crystal Barel experiment. The maximum magnetic field is 2 T and corresponds to a current of about 1500 A. For the hodoscope, scintillation counters are used which consists of plastic scintillators and photomultipliers. The scintillators are installed half overlapping. This kind of detectors allow a fast and precise measurement of the timing of the incoming scattered electrons. A prototype of the hodoscope was constructed by Georg Siebke [Sie10] which is shown in figure 3.4 The readout electronics is currently being developed by Francessco Messi [Mes11]. Due to spatial limitations, the hodoscope cannot be placed completly in the focal

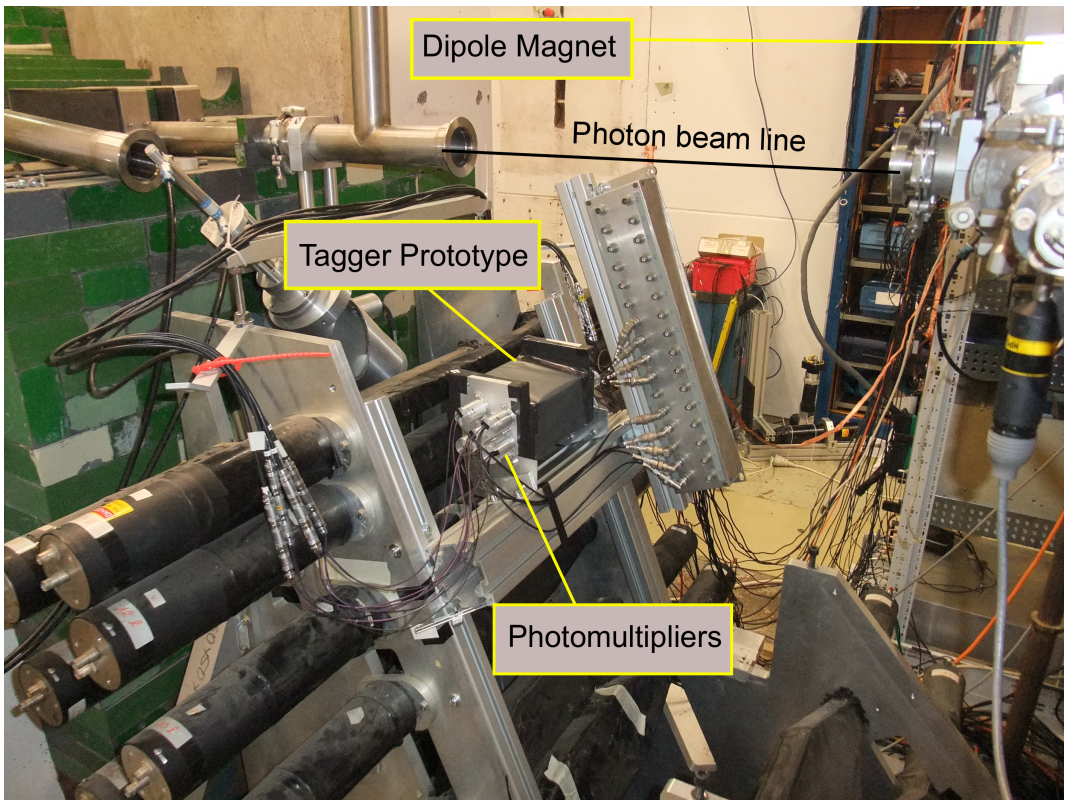

Figure 3.4: Tagging prototype implemented in the BGO-OD tagging system [Sie10]

plane of the tagging magnet. The final setup of the hodoscope will be split up into two different parts. With an energy for the incident electron beam of about $E_0 = 3.2\,\text{GeV}$, the hodoscope can be placed into the focal plane for energies of scattered electrons up to $E_{sca} \approx 1220\,\text{MeV}$, while for larger electron energies the

detector have to be aligned in the vertical plane in front of the tagging magnet. This setup is shown in figure 3.5. The energy resolution, which can be achived by the focal plane is about $\sigma_E = 0.19\% E_0 \approx 6\,\mathrm{MeV}$. For higher electron energies trajectories with same energy difference become closer to each other. The consequence is that the scintillators must also move closer together to maintain a constant energy resolution. Since, the spatial size of the photomultipliers, which are placed on the outside of the hodoscope, as illustrated in figure 3.4, prevents an arbitrarily compact arrangement of the scintillators, larger scintillator bars are used at electron energies of $E = 60.6\% E_0 \approx 1940\,\mathrm{MeV}$ and $E = 74.4\% E_0 \approx 2380\,\mathrm{MeV}$. This results in a decrease of the energy resolution of the hodoscope in the vertical plane, which is presented in figure 3.6. A more detailed description of the tagging system can be found in [Sie10]

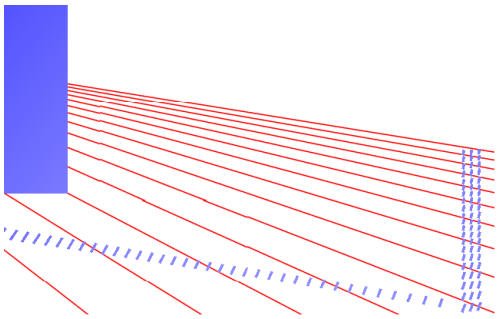

Figure 3.5: Calculated detector layout with variable energy resolution [Sie10]. The red tracks describe the electron trajectories with steps of 200MeV.

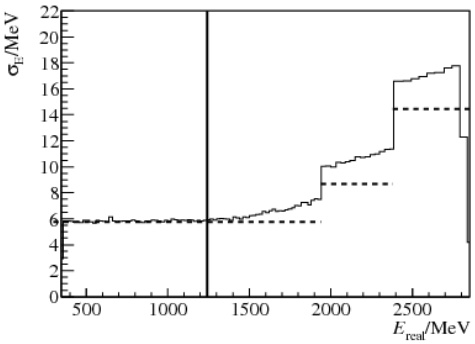

Figure 3.6: Simulated energy resolution[Sie10]. The vertical line denote the end of the focal plane. The horizontal lines denote the theoretical minimum resolution due to the energy width.

4 The Goniometer System

In the BGO-OD experiment, the process of bremsstrahlung is used to produce highly energetic photon beams. Therefore, accelerated electrons are shot on a thin metal radiator, e.g. copper. In order to have the optia to switch between radiators of different thicknesses and materials, these radiators are fixed on a round plate, which is mounted on a multiple dimension positioning goniometer. For a more precise examination of the excitation spectra of nuclei, linearly and circularly polarised photons have to be used. Linear polarised photons can be produced by taking advantage of the process of coherent bremsstrahlung. Therefore, a crystal, e.g. diamond has to be used. Because the degree of polarisation depends strongly on the orientation of the crystal with respect to the primary electron beam, the crystal has to be aligned precisely by the goniometer [Els07]. Generally a positioning goniometer is an instrument to rotate an object precisely in one dimension around the roation axis of the goniometer stage. Combining different kinds of positioning goniometers allows a precise alignment of the crystal in all spatial dimensions. The different parts of the goniometer system which was setup in the framework of this thesis are introduced in this chapter.

4.1 The Goniometer

The goniometer used in this experiment, consists of two translation and three rotation stages from *Newport* [New], which allows translation perpendicular to the beamline in the vertical and horizontal plane and rotations around all three spatial axes. The relevant technical specifications are listed in table 4.1 and 4.2
The goniometer uses, stepper motors, e.g. [New1], which do not require encoders. Relative positions are approached by the number of commanded steps. Using a newport motion controller allows a dynamic micro-stepping mode, which increases the sensitivity to one hundredth of a normal step [New2]. To know the absolute positions, the stages have to find a reference position first, which is realised by an optical transition.

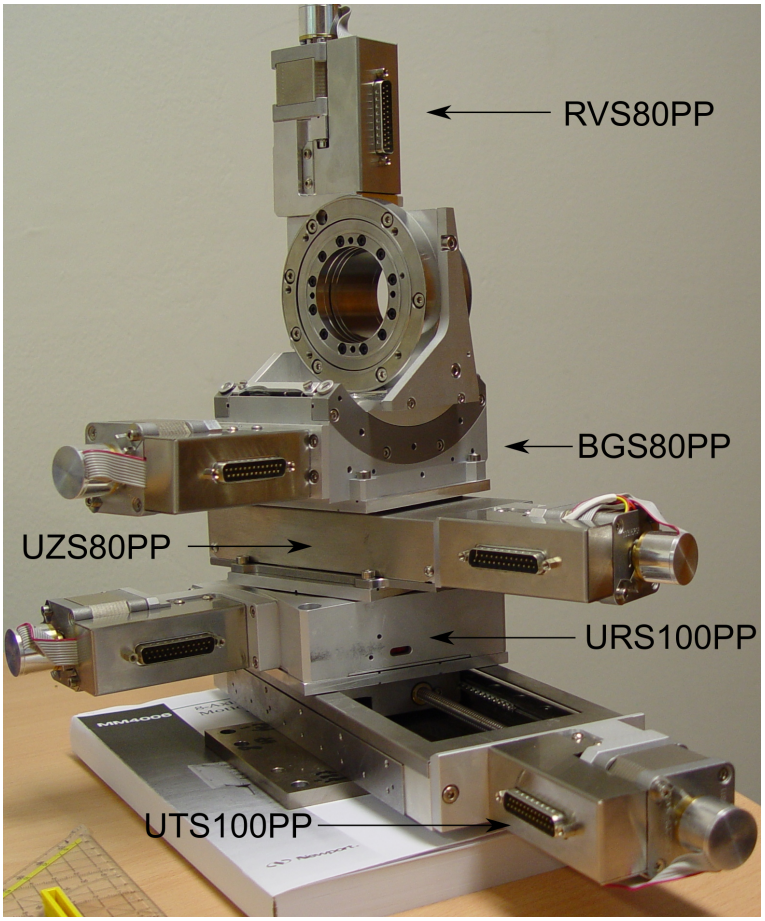

Figure 4.1: The Goniometer used in the BGO-OD experiment without radiators.

A Controller of type XPS from Newport is used for controlling the goniometer, which can be equipped with seperate driver cards to use up to eight different motion stages at the same time. The operation of the controller is possible via an Ethernet 10/100 Base-T interface. A pre-installed web interface is used for the configuration and controlling of the motion stages. The configuration will be done only once with a web interface, whereas the controlling of the motion stages is done by the experimental control [Han11]. Because the goniometer will be setup in a scattering chamber, it is necessary to set limits to the traveling rangeswith the controller to exclude collisions with the inner wall of the tank. In addition, hardware limit switches are implemented to prevent accidents in case of any software malfunction. The crystal will be placed in the intersection point of the axis of the ration stages. Diagnosis elements to examine the primary electron beam and different amorphous radiators, which will be presented in section 4.3, are placed on an aluminium plate with a diameter of 24 cm and thickness of 1 cm, which is fixed with an aluminium

	UTS150PP	UZS80PP
travel range	150 mm	4.5 mm
resolution	0.1 μm	0.01 μm
hysteresis	5 μ	3 μm
uni directional rep.	1 μm	1.4 μm
limit switches	opt. $\pm$75 mm	opt. $\pm$2.25 mm

Table 4.1: Linear motorised goniometer stage specifications [New]

	URS100BPP	BGS80PP	RVS80PP
travel range	360°	$\pm$45°	360°
resolution	0.0002°	0.0001°	0.0001°
hysteresis	0.006°	0.004°	0.005°
uni directional rep.	0.016°	0.001°	0.002°
limit switches	opt. $\pm$6°	mech. $\pm$45°	opt. $\pm$170° , can be deactivated

Table 4.2: Rotational motorised goniometer stage specifications [New]

tube at a distance of 60.8 mm on the azimuthal rotation stage. The tube has an inner radius of 22.5 mm and a wall thickness of 5 mm.

4.2 Verifying some Specifications of the Goniometer

To minimize the systematical errors of the determination of the degree of polarisation due to inadequate positioning of the crystal, the rotation stages which are responsible for the horizontal θ_h and vertical θ_v rotation were checked for their specifications by G.Siebke and T.Schwan. A method described by A. Schmidt [Sch95] was used.

A mirror was placed in the intersection point of the axis of the rotation stages. With a He-Ne laser, the angle of rotation is projected on a wall in a distance of 11.24 m as shown in figure 4.2. The error for the determination of the laser's position was assumed to be 0.5 mm. The resulting angular resolution relates with 0,001° to the resolution of the encoder. The measured specifications are listed in table 4.3 and 4.4 and compared to the data which are given by Newport. The correlation between the projected distances and the angles (figure 4.2) of rotation are given by

$$\phi_V = \frac{1}{2}\left[\arctan\left(\frac{x_V}{d} + \tan\theta\right) - \theta\right] \quad ; \quad \phi_H = \arctan\left(\frac{x_H}{2d}\right). \tag{4.1}$$

	Specification	Laser test
repetition accuracy	0.001°	$\leq$ 0.0007°
hysteresis	0.006°	$\leq$ 0.0013°
uni directional rep.	0.016°	$\leq$ 0.0037°

Table 4.3: Stage: URS100BPP, vertical rotation

	Specification	Laser test
repetition accuracy	0.001°	$\leq$ 0.0007°
hysteresis	0.004°	$\leq$ 0.0013°
uni directional rep.	0.006°	$\leq$ 0.0048°

Table 4.4: Stage: BGS80PP, horizontal rotation

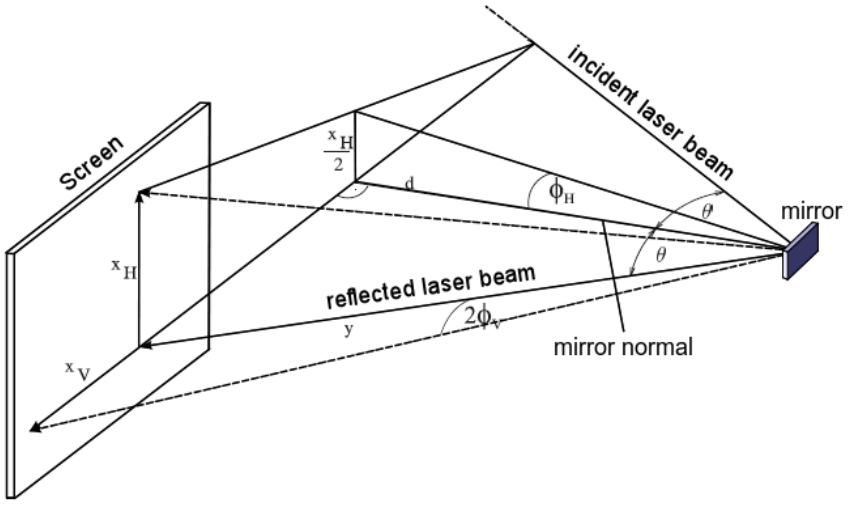

Figure 4.2: Principle of the laser test for the verification of the goniometer specifications [Sch95].

4.3 Radiator Plate

To use different amorphous radiators and tools for the examination of the primary electron beam, they are mounted on an aluminium plate, which is fixed on the azimuthal rotation stage RVS80PP (figure 4.1). In this aluminium plate, three copper strips with different thicknesses and one capton foil are placed . To determine the beam profile, two nickel-steel wires are used. These wires are aligned in the vertical and horizontal plane perpendicular to the primary electron beam. To measure the beam profile. The wires are moved horizontally and vertically through the electron beam. The electrons produce bremsstrahlung and are detected by the tagging

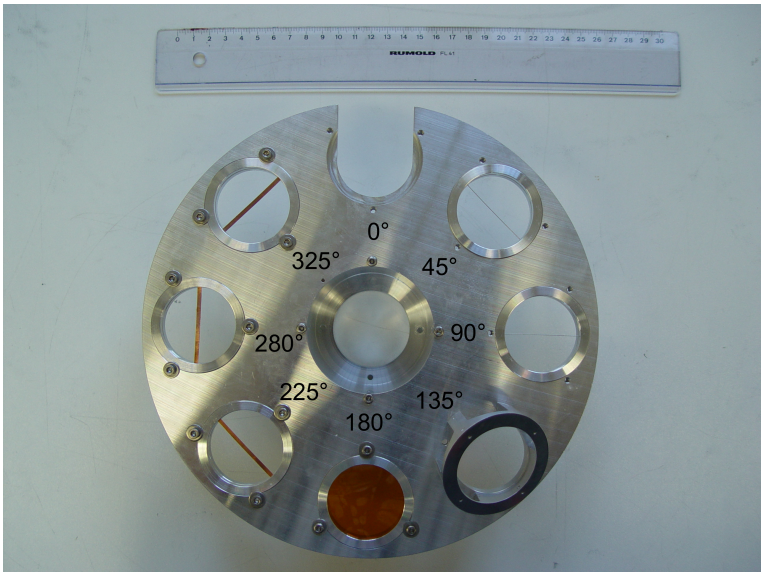

Figure 4.3: The aluminium plate with the radiators and intruments for the examination of the primary electron beam.

Position	0°	45°	90°	135°
Utensil	empty	v. wire 250μm	h. wire 250μm	chromox plate
Position	180°	225°	280°	325°
Utensil	capton foil 125μm	copper 50μm	copper 150μm	copper 200μm

Table 4.5: Radiators and tools for beam inspection

hodoscope. The bremsstrahlung production rate depends on the position of the wire in the electron beam, beacuse the electron concentration in the middle of the electron beam is much higher as at the edge. This makes the measurement of the beam profile possible.

Each utensil is glued with UHU plus endfest 300 between two rings of aluminium, which have a diameter of 46 mm. For a fast verification of the beam position a luminescence screen made of chromox is fixed with an angle of 45° to the beam. This allows the obversation of the beam with a camera at an angle of 90°. Details of the radiators and wires can be found in table 4.5. The crystal will be fixed on the other side of the azimuthal rotational stage. For this experiment a diamond crystal will be used. The advantage compared to other crystals will be discussed in chapter 5.

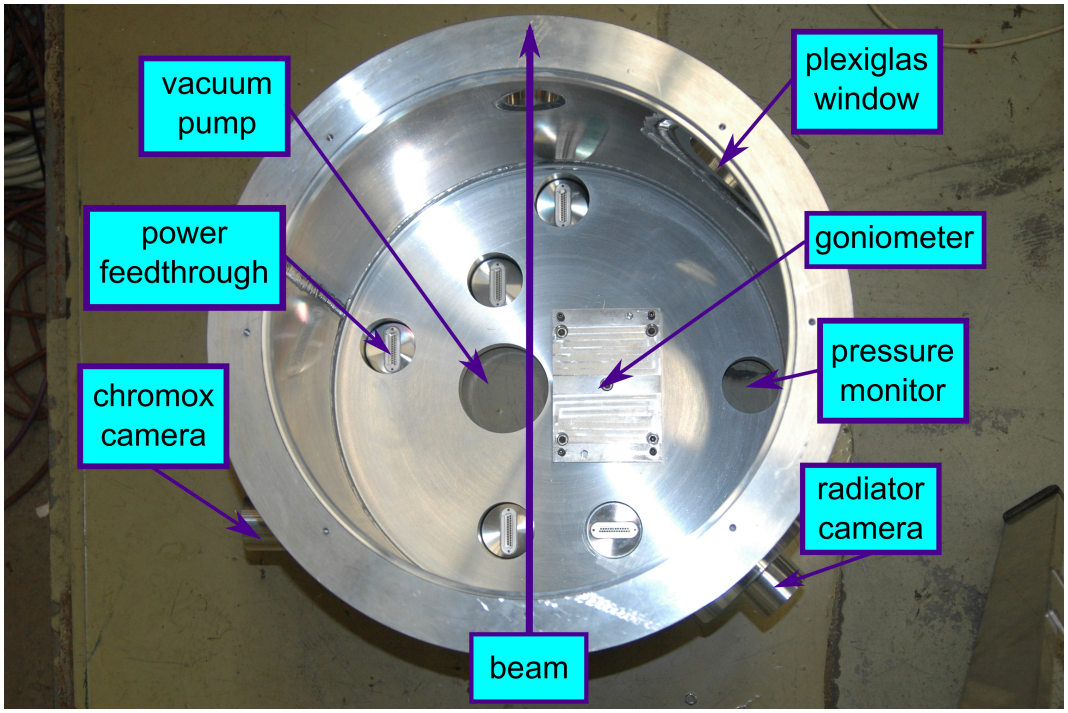

Figure 4.4: The vacuum tank from above.

4.4 Vacuum Tank

A scattering chamber with a vacuum which is used in this experiment. The gonimeter is placed on a plateau in the scattering chamber and adjusted to the position of the position of the electron beam. To ensure repeatability of positioning of the goniometer it is fixed with dowel pins. It includes connections for two cameras. One connection is attached at an angle of 90° to the electron beam to oberserve the electron beam impinging on the chromox plate. The other one is used for observing the radiator plate, which is mounted at an angle of 45° to the electron beam on the tank. In addition a plexiglas window was mounted on the outside of the vacuum. In order to illuminate inside the tank, a light source is placed in front of the plexiglas window. On the lower side of the vacuum tank five vacuum qualified power feedthroughs for the goniometer, one connection for the vacuum pump and one for the pressure monitor are placed. The construction of the tank can be seen in figure 4.4.

5 Bremsstrahlung

Photoproduction experiments like the BGO-OD experiment use a highly energetic photon beam to excite baryons. The photon beam is produced via bremsstrahlung of an electron beam. Using an amorphous radiator leads due to rotational symmetry to an effectivly non linearly polarised photon beam. Taking advantage of the coherent bremsstrahlung process by using a crystal instead of an amorphous radiator, production of linearly polarised photons is possible. In this chapter the kinematical conditions and the cross sections for the incoherent bremsstrahlung process will be presented first. The second part of this chapter will deal with the modification of the cross section for the coherent bremsstrahlung process followed by the calculations for the determination of the degree of polarisation. Due to the fact that the degree of polarisation depends strongly on the orientation of the crystal with respect to the primary electron beam, the necessary conditions of the crystal's orientation are described at the end of this chapter.

5.1 Incoherent Bremsstrahlung

By the deflection in an electromagnetic field, electrons become accelerated and lose energy by the process of bremsstrahlung. Due to this process, one or more real photons are produced. Because of momentum conservation, the presence of a third particle (i.e. a nucleus), which takes a certain recoil momentum, is necessary. Figure 5.1 shows the possible Feynman Graphs for the process of bremsstrahlung in the lowest order. The electrical field vector of the bremsstrahlung photon lies in the plane which is spanned by the recoil momentum and the momentum of the incident electron. If an amorphous radiator is used for the production of incoherent bremsstrahlung, the distribution of collisions and the recoil orientation are isotropic meaning that no scattering planes are distinguished. This leads to no effective linear polarisation of the photon beam.

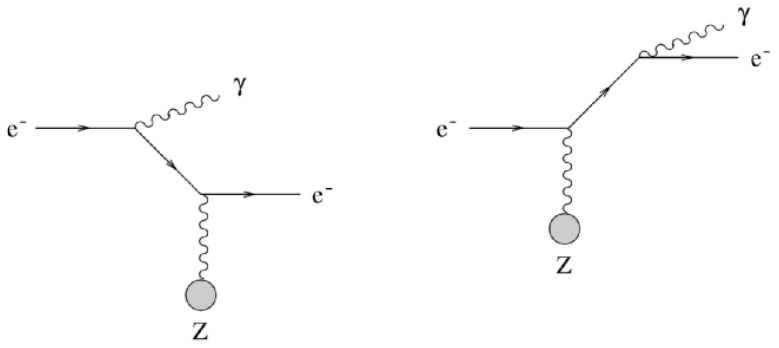

Figure 5.1: Feynman graphs of second order for the bremsstrahlung process of an electron on a nucleus with atomic number Z.

5.1.1 Kinematics

The following relations

$$E_0 = E + k + T \tag{5.1}$$

$$\vec{p_0} = \vec{p} + \vec{k} + \vec{q} \tag{5.2}$$

describe the kinematic conditions for the bremsstrahlung process:

$$e^- + N \rightarrow e^- + N + \gamma$$

where:

$$\begin{aligned} E_0,\ \vec{p_o} &= \text{energy and momentum of the incident electrons} \\ E,\ \vec{p} &= \text{energy and momentum of the outgoing electrons} \\ k, \vec{k} &= \text{energy and momentum of the bremsstrahlung photon} \\ T, \vec{q} &= \text{recoil energy an momentum of the collision partner} \end{aligned}$$

For recoil momenta of $q \approx mc$, the recoil energy of $T = q^2/2M_N \approx 10^{-5}\,\text{MeV}$ can be neglected. N describes a scattering partner which is a nucleon in this case, e^- the electron and γ the emitted bremsstrahlung photon.
Due to rotational symmetry related to the direction of the incident electrons it is

possible to split the recoil momenta into longitudinal and transverse components, q_l and q_t, which is shown in figure 5.2.

$$q_l = p_0 - p\cos\theta_e - k\cos\theta_k \tag{5.3}$$
$$q_t^2 = p^2\theta_e^2 + k^2\theta_k^2 + 2pk\theta_e\theta_k\cos\psi \tag{5.4}$$

with:

$$\theta_e = \angle(\vec{p}_0, \vec{p}) \tag{5.5}$$
$$\theta_k = \angle(\vec{p}_0, \vec{k}) \tag{5.6}$$
$$\psi = \angle(\vec{p}_0, \vec{p})(\vec{p}_0, \vec{k}) \tag{5.7}$$

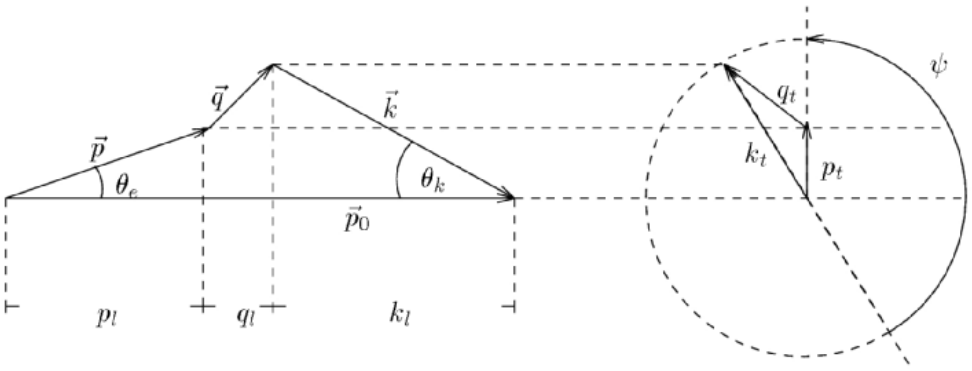

Figure 5.2: Kinematics of the bremsstrahlung process, splitted into longitudinal and tranversal components.

Not any recoil momentum can be absorbed by the nucleus. In the following the kinematical constraint for the recoil will be discussed [Tim69]. In the case of incident high energy electrons, the photon will be emitted in a forward direction. For $\theta_e = \theta_k = 0$, the transverse component of the recoil momentum tends to zero, while a sharp lower limit for the longitudinal component is obtained. This limit depends on the energy of the incident electron and of the emitted bremsstrahlung photon. For high energies the following approximation can be made[1]:

$$p = \sqrt{E^2 - 1} \sim E - \frac{1}{2E} \quad \text{for} \quad (E_0, E \gg 1). \tag{5.8}$$

[1]The units which are used are given in the appendix A.1.

By using the relative photon energy $x = \frac{k}{E_0}$ the lower recoil boundary for the longitudinal component is given by:

$$\delta(x) \equiv q_l^{min} = \frac{1}{2E_0}\frac{x}{1-x}. \tag{5.9}$$

And therefore

$$p\sin\theta_e = k\sin\theta_k. \tag{5.10}$$

If θ_k is replaced by the characteristic opening angle $\theta_\gamma = m_e/E_0$ in equation 5.3 and if q is negligible compared to p_0, p and k, using small angle approximation leads to an electron emission angle which is given by

$$\theta_e = \frac{k}{EE_0} = \frac{1}{E_0}\frac{x}{1-x}. \tag{5.11}$$

If θ_e and θ_k are used in equation 5.3 together with $p = E$ for high electron energies and $\cos\theta = 1 - \theta^2/2$ for small angles, an upper limit for the longitudinal recoil component can be recieved:

$$q_l^{max} \approx \frac{1}{E_0}\frac{x}{1-x} = 2\delta. \tag{5.12}$$

Which gives the relation

$$\delta \leq q_l \lesssim 2\delta.$$

The transverse component is at a maximum at $\psi = 0$ (s. page 29) and minimum at $\theta_e = \theta_k = 0$. For q_t the following boundaries are given as

$$0 \leq q_t \leq 2x.$$

The lower limit of the longitudinal component was approximated with $q_t = 0$, but q_t can be bigger than q_l. A general forumlation for the limits of the transverse and londitudinal components is therefore needed. The results of a more detailed calculation which is given in [Tim69] are presented here. For a fixed value of q_l, the maximum value of the transverse component is given by

$$q_t^{max} = \sqrt{2E_0(q_l - \delta)}. \tag{5.13}$$

The new limits are

$$\delta + \frac{(q_t^{max})^2}{2E_0} \leq q_l \leq \frac{\delta}{x} \tag{5.14}$$

$$0 \leq q_t \leq 1 = q_t^{max} \tag{5.15}$$

These limits describe a kinematically allowed region called a "pancake", which is shown in figure 5.3.

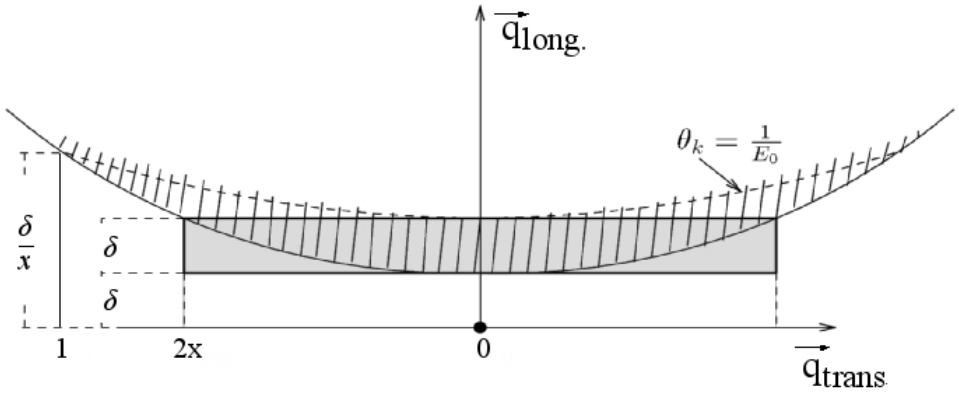

Figure 5.3: Kinematic constraints of the bremsstrahlung process. The grey rectangle describes the approximation, while the hatched curved shape corresponds to the exact calculation. Due to $q_l \ll q_t$, the pancake is not shown to scale. The upper smooth limit is estimated by $\theta_k = \frac{1}{E_0}$

For a fixed longitudinal recoil momentum, it is now possible to calculate a maximum relative photon energy for which the recoil momentum is still lying in the kinematically allowed region. This is given by

$$x_d = \frac{2E_0 q_l}{1 + 2E_0 q_l}. \tag{5.16}$$

The cross section falls to zero if the relative photon energy is higher than x_d.

5.1.2 The incoherent Cross Section

The cross section of a scattering process is desribed by

$$\sigma = \frac{|M_{if}| \cdot \text{phase space factor}}{\text{time} \cdot \text{particle flux}} \tag{5.17}$$

$|M_{if}|$ defines the matrix element, which decribes the possibility of the scattering process. In the case of incoherent bremsstrahlung, it applies by E. Haug [Hau04]

$$\frac{d^3\sigma}{dkd\Omega_k d\Omega_p} = \frac{\alpha}{(2\pi)^4}\frac{E_0 E p k}{p_0}\left(\frac{\hbar}{mc}\right)^2 |M_{if}|^2 \tag{5.18}$$

A more detailed calculation for the matrix element can be found in [Hau04].

$$\begin{aligned}\frac{d^3\sigma_B}{dkd\Omega_k d\Omega_p} = \frac{\alpha Z r_0^2}{4\pi^2}\frac{p}{k p_0 \mathbf{q^4}}\Bigg(& (4E^2 - q^2)\frac{p_0^2 \sin^2\theta_0}{(E_0 - p_0\cos\theta_0)^2}(4E_0^2 - q^2)\frac{p^2\sin^2\theta}{(E - p\cos\theta)^2} \\ & + (4E_0 E - q^2 + 2k^2)\frac{2p_0 p\sin\theta_0 \sin\theta\cos\phi}{(E_0 - p_0\cos\theta_0)(E - p\cos\theta)} \\ & + 2k^2\frac{p_0^2\sin^2\theta_0 + p^2\sin^2\theta}{(E_0 - p_0\cos\theta_0)(E - p\cos\theta)}\Bigg)\end{aligned} \tag{5.19}$$

with:

$$\begin{aligned}\alpha &= \text{electromagnetic coupling constant} \\ Z &= \text{Recoil partner} \\ p_0, E_0 &= \text{Momentum and energy of incident electron} \\ p, E &= \text{Momentum and energy of scattered electron} \\ k &= \text{Energy of the bremsstrahlung photon} \\ q &= \text{Transferred recoil momentum} \\ \theta_0 &= \text{Photon opening angle} \\ \theta &= \text{Scattered electron opening angle} \\ \phi &= \text{Angle between } p_0 \text{ and } p.\end{aligned}$$

This cross section is also known as Bethe-Heitler cross section. The dependence of the cross section on the fourth power of the recoil momentum explains why small recoil momenta contribute more than high recoil momenta to the cross section. An integration over all emission angles leads to the spectral distribution [Lan86]

$$d\sigma_{B.H.} = 4Z^2\alpha a_0^2\frac{dk}{k}\frac{E}{E_0}\left[\frac{E_0}{E} + \frac{E}{E_0 - \frac{2}{3}}\right]\left[ln\left(\frac{2E_0 E}{k}\right) - \frac{1}{2}\right]. \tag{5.20}$$

In a first approximation the bremsstrahlung spectrum is proportional to $1/k$.

5.1.3 Screening of the Coulomb Potential of the Nucleon

Because small recoil momenta have a lager effect on the cross section than higher ones, it needs to be proven if the corresponding distance $r \approx 1/q$ is larger than the radius R of the Atom, which is given by $a_0 Z^{-1/3}$ with $a_0 = Bohr\ radius$. In this case, screening effects of the nucleus by the shell electrons has to be considered. The minimum recoil momentum is given by

$$|\vec{q}_{min}| = |\vec{p_0}| - |\vec{p}| - |\vec{k}| \sim \frac{k}{2E_0E}. \tag{5.21}$$

For typical electron energies E_0 which can be achieved at ELSA, the corresponding distance can be bigger than the radius of the nucleous

$$r = \frac{1}{|\vec{q}_{min}|} \sim \frac{2E_0E}{k} > a_0 Z^{-\frac{1}{3}} \tag{5.22}$$

and the effect of screening has to be considered. To do this, the nuclear charge density has to be replaced by an effective charge density, which consists of the electron charge $en(\vec{r})$ and the nuclear charge $Ze\delta(\vec{r})$

$$\rho(\vec{r}) = -en(\vec{r}) + Ze\delta(\vec{r}). \tag{5.23}$$

After a Fourier transformation in momentum space, the nuclear charge Z has to be replaced by $Z[1 - F(q)]$. The screened Coulomb-Potential in momentum space is than given by

$$V(q) = \frac{4\pi e^2}{q^2}(Z - F(q)). \tag{5.24}$$

Here $F(q)$ indicates the atomic form factor which describes the charge distribution of the shell electrons and thus the screening of the nucleus

$$F(q) = \int \rho(r) e^{-i\vec{q}\vec{r}} d^3r. \tag{5.25}$$

For a numerical calculation of the atomic form factor, L.I. Schiff [Sch51] assumed an exponential screening potential

$$V_s(r) = -\frac{Ze^2}{r} e^{-\frac{r}{\beta}} \quad \text{with} \quad \beta = C \cdot Z^{-\frac{1}{3}} \ ; \ C = 111. \tag{5.26}$$

Where β describes the screening radius and C the screening constant. The fourier transformation of this potential leads to

$$V_s(q) = -\frac{4\pi Z e^2}{q^2 + \beta^{-2}}. \tag{5.27}$$

This results in the following atomic form factor

$$F(q) = (q^2 + \beta^{-2})^{-2}. \tag{5.28}$$

To consider the effect of screening in the differential cross section, the charge distribution of the electrons gets seperated from the nuclear potential, by rewriting the atomic form factor as

$$F(q) = \left(\frac{V(q)}{4\pi Z e^2}\right)^2 \left(1 - \frac{1}{1 + (q\beta)^2}\right)^2 = \frac{1}{q^4}(1 - F'(q))^2. \tag{5.29}$$

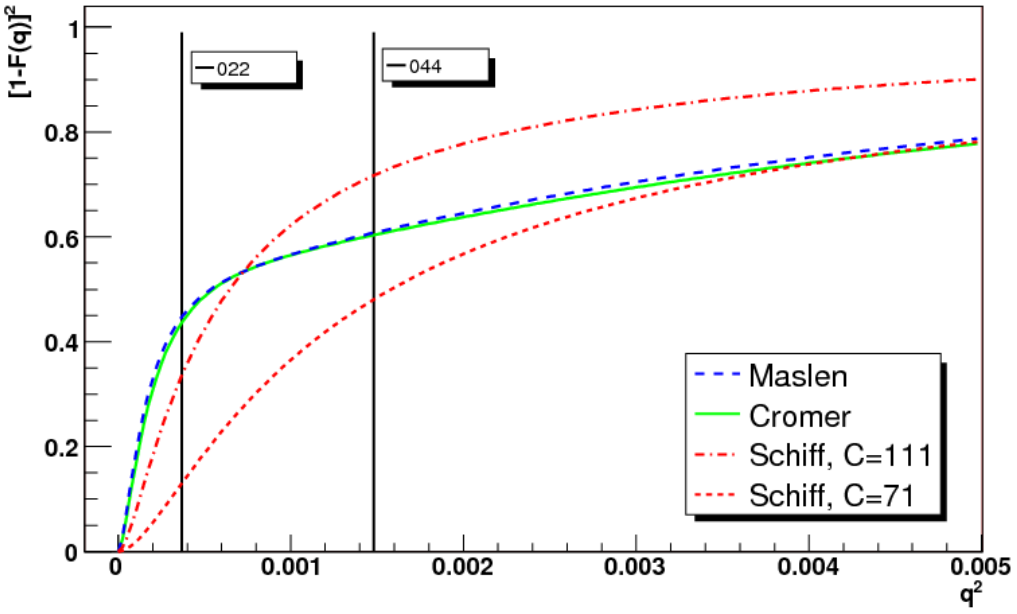

Figure 5.4: Comparison of different parameterisations of the atomic form factor [Els07]. In red and line-dotted is shown a dipole form factor according to Schiff [Sch51] with a shielding constant of $C = 111$ and according to Timm [Tim69], in red dotted with $C = 71$ for $q^2 \leq 0.01$. In blue the parameterisation determined by Maslen [MFO92] and in green by Cromer [CW65]. The vertical lines indicate typical values for recoil momenta, which corresponds to the [022] and [044] reciprocal lattice vectors (chapter 5.2)

The approximation of the form factor by equation 5.27, to describe experimental data is not sufficient. A better parameterisation of the form factor, which is used in this diploma theses, was established by Maslen [MFO92]. It is similiar to the parameterisation of Cromer [CW65]. These form factors, are illustrated and compared in figure 5.4 . Generally the parameterisations of Cromer and Maslen yield smaller values for the form factor compared to Schiff, but it is possible to adjust this deviation by choosing another screening constant $C = 71$ for $q^2 \gtrsim 0,01$.

5.2 Coherent Bremsstrahlung

Up to now, only the process of incoherent bremsstrahlung has been discussed, which can be described by the Bethe-Heitler cross section, leading to non linearly polarised photons. For the investigation of the exitation spectrum of the nuclei, it is necessary to use polarized photons, which can be produced by the effect of coherent bremsstrahlung. This can be achieved using a crystalline radiator, due to the periodical arrangement of the atoms. The orientation of the crystal related to the primary electron beam is of great significance. Because of the lattice structure of the crystal, the cross section has to be modified. Furthermore the determination of the degree of polarisation will be dicussed.

5.2.1 Kinematics

The periodic arrangement of the atoms in the lattice of a crystal radiator allows under certain conditions constructive interference between the bremsstrahlung amplitudes of individual atoms. In comparison to the incoherent bremsstrahlung, the recoil momentum gets absorbed recoilless by the hole crystal, with a mass much higher than the mass of a single atom, similar to the Mößbauer effect [Moe58]. Therefore the recoil energy can be neglected. As the photon gets produced in a process where many atoms are involved, this process is called “coherent”. Similar to the scattering of X-rays, only for recoil momenta which are equal to a multiple of a reciprocal lattice vector, the process of coherent bremsstrahlung has to fullfill the Laue-Bragg condition

$$\vec{q} = n \cdot \vec{g}. \tag{5.30}$$

Here $\vec{q}$ denotes the recoil momentum and $\vec{g}$ a reciprocal lattice vector. Demonstratively a reciprocal lattice vector describes a group of parallel planes in position space, while the components of the reciprocal lattice vector are given by the Miller

indices [Kit06]. As shown in equation 5.19, small recoil momenta contributes more to the cross section. Due to the preferred small recoil momenta small lattice vectors contribute more to the cross section. As in the case of incoherent bremsstrahlung, the recoil momenta has to be remain within the kinematical allowed region (pancake). If this condition is not fullfilled, the cross section vanishes.

5.2.2 The Coherent Cross Section

Due to the crystal structure it is necessary to modify the cross section for the production of coherent bremsstrahlung. Real crystals have lattice defects and due to thermal excitation, zero-point oscillations, leading to different and fluctuating displacments of the atoms. Incoherent bremsstrahlung is therefore also produced. The cross section of bremsstrahlung, from a crystal, can be written as follows:

$$d\sigma_{crystal} = d\sigma_{coherent} + d\sigma_{incoherent}. \tag{5.31}$$

The modification of the cross section will be discussed in the next paragraphs.

- **The Debye-Waller factor**
  The periodicity of the lattice is disturbed by zero-point oscillations due to thermal excitations. This causes a reduction of the momentum transfer to the lattice, and therefor a reduction of the coherent bremsstrahlung by a factor f, which is given by
  $$f(q^2) = e^{-A(T)q^2}. \tag{5.32}$$
  $A(T)$ describes the mean displacments of the atoms:
  $$A(T) = \frac{3m_e^2c^2}{4Mk_b\Theta}\left[1 + 4\frac{T}{\Theta}\Psi\left(\frac{\Theta}{T}\right)\right]. \tag{5.33}$$
  Where M is the mass of the atom, m_e the electron mass, k_b Boltzmann constant, T the temperature and Θ the Debye temperature. $\Psi(\frac{\Theta}{T})$ is the Debye function, which is defined in [Lau60]
  $$\Psi\left(\frac{\Theta}{T}\right) = \frac{T}{\Theta}\int_0^{\frac{\Theta}{T}} \frac{tdt}{e^t - 1} \tag{5.34}$$
  The incoherent part contributes with $(1 - f)$ to the crystal cross section. According to equation 5.32 and 5.33, the Debye-Waller factor decreases with

increasing temperature. An improvement of the coherent bremsstrahlung contribution can be achieved by choosing a crystal with a high Debye temperature. Diamond with $\Theta = 2230K$ is a suitable choice, compared to Beryllium with $\Theta = 1160K$ and Silizium with $\Theta = 640K$.

- **The diffraction factor**
  Because the electrons scatter in a crystal, several atoms acts as scattering center at the same time. The diffraction factor considers the scattering process on many atoms. If N atoms are involved in the scattering process, the resulting amplitude is the sum of the incoming and outgoing plane wave over all scattering centers [Tim69]. By squaring the resulting amplitude, the differential cross section can be written as

$$d\sigma_N(\vec{q}) = |\Phi_N(\vec{q})|^2 = \left|\sum_{i=1}^{N} e^{i(\vec{r},\vec{q})}\right|^2 \cdot |\Phi(q)|^2 = D(\vec{q}) \cdot d\sigma(\vec{q}). \tag{5.35}$$

  Because the distribution of atoms in an amorphous material is arbitrary, the diffraction factor is given by the number N of atoms which exist in the radiator. For a crystalline radiator, the diffraction factor can be written as

$$D(\vec{q}) = \left(\frac{2\pi}{a}\right)^3 \sum_{h_{kl}} \prod_{k=1}^{3} N_k \cdot \delta\left(q_k - \frac{2\pi h_{kl}}{a}\right). \tag{5.36}$$

  Here a denotes the lattice constant and h_{kl} the Miller indices of the reciprocal lattice vector. A detailed calculation of the diffraction factor of the crystal can be found in [Tim69]. The δ-function works like the Laue-Bragg condition, which only allows scattering processes, where the recoil momentum is equal to a multiple of a reciprocal lattice vector.

- **The structure factor**
  It is possible, that the contributions of lattice planes interfere destructively with each other. This effect is taken into account by the structure factor $S(\vec{g})$. The structure factor for diamond, according to [Tim69], is given by

$$S(\vec{g}) = [1 + e^{i\pi/2(h_1+h_2+h_3)}][1 + e^{i\pi(h_2+h_3)} + e^{i\pi(h_3+h_1)} + e^{i\pi(h_1+h_2)}]. \tag{5.37}$$

  Here h_i are the components of the reciprocal lattice vector $\vec{g}$. The selection rules for the structure factor are

  1. $|S(\vec{g})| = 64$, if h, k, l are even and (h + k + l) can be divided by four.

2. $|S(\vec{g})| = 32$, if h, k, l are odd

3. $|S(\vec{g})| = 0$ for all other cases.

Using equations 5.36 and 5.37, the cross section 5.35 can be written as:

$$d\sigma_N(\vec{q}) = \left(\frac{2\pi}{a}\right)^3 \frac{N}{8} \left[\sum_{g_\nu} |S(\vec{g})| \cdot \delta(\vec{q} - \vec{g_\nu})\right] \cdot d\sigma(\vec{q}). \tag{5.38}$$

- **The resulting coherent cross section**
  After considering all effects which are listed above, the cross section for coherent bremsstrahlung on a diamond can be written as

$$d\sigma_{crystal}(\vec{q}) = \left[\frac{1}{8}\left(\frac{2\pi}{a}\right)^3 e^{-Aq^2} \sum_{g_\nu} |S(\vec{g})|^2 \cdot \delta(\vec{q} - \vec{g_\nu}) + (1 - e^{-Aq^2})\right] \cdot d\sigma(\vec{q}) \tag{5.39}$$

$$= d\sigma_{coherent} + d\sigma_{incoherent}. \tag{5.40}$$

5.3 Intensity Distribution of Incoherent and Coherent Bremsstrahlung

Using a crystal radiator, the relative intensity distribution of bremsstrahlung can be written, according to U. Timm [Tim69] and G. Diambrini [Dia68], as the sum of the cross sections which includes the linear polarised contributions perpendicular σ_{perb} or parallel $\sigma_{parallel}$ to a reference plane

$$I = \frac{k}{\sigma_0}\frac{d\sigma_{cry}}{dk} = \frac{k}{\sigma_0}\frac{d\sigma^{||} + d\sigma^{\perp}}{dk} = (1 + (1-x)^2)(\Psi_1^c + \Psi_1^{inc}) - \frac{2}{3}(1-x)(\Psi_2^c + \Psi_2^{inc}) \tag{5.41}$$

With $\sigma_0 = (\frac{Z^2}{137})(\frac{e^2}{mc^2})^2$ and k = photon energy. The incoherent distribution is decribed by the functions $\Psi_{1,2}^{inc}$ which are given as

$$\Psi_1^{inc} = 4 + 4\int_\delta^1 (1 - e^{-Aq^2}) F(q^2)(q-\delta)^2 q dq, \tag{5.42}$$

$$\Psi_2^{inc} = \frac{10}{3} + 4\int_\delta^1 (1 - e^{-Aq^2}) F(q^2) \left(q^2 - 6\delta^2 \ln\frac{q}{\delta} + 3\delta^2 - 4\frac{\delta^3}{q}\right) dq. \tag{5.43}$$

In addition to the incoherent distribution the intensity distribution of shell electrons, which is called the electron-electron bremsstrahlung also has to be considered. According to Wheeler and Lamb [WL39], these contributions are given as $\Psi_1^{inc,e} = 4.1$ and $\Psi_2^{inc,e} = 4.0$. and have to be added to Ψ_1^{inc} and Ψ_2^{inc}.

The functions $\Psi_{1,2}^c$ describe the coherent contribution and are defined by

$$\Psi_1^c = \frac{1}{2}\frac{(2\pi)^2}{a^3}\delta \sum_{\vec{g}} |S(\vec{g})|^2 e^{-Ag^2} \frac{(1-F(g^2))^2}{g^4}\frac{q_t^2}{q_l^2} \tag{5.44}$$

$$\Psi_2^c = 3\frac{(2\pi)^2}{a^3}\delta^2 \sum_{\vec{g}} |S(\vec{g})|^2 e^{-Ag^2} \frac{(1-F(g^2))^2}{g^4}\frac{q_t^2(q_l-\delta)}{q_l^4}. \tag{5.45}$$

The summation is only performed over reciprocal lattice vectors which are located inside the *pancake* area. As mentioned before it is possible to determine a certain relative photon energy x_d for each lattice vector where the cross section falls discontinuously to zero. The intensity distribution has its maximum at $x = x_d$, because Ψ_2^c is zero due to $q_l = \delta$. The resulting intensity distribution at the discontinuity for different reciprocal lattice vectors is given by

$$I_{x_d}^c = \chi(x_d) \cdot E_0 \frac{(2\pi)^2}{a^3}|S|^2 e^{-Ag^2} g^2 F(g^2) \tag{5.46}$$

with

$$\chi(x_d) = [1 + (1-x_d)^2](1-x_d)/x_d. \tag{5.47}$$

The enveloped curve is shown in Figure 5.5, which grows for $x_d \to 0$, but falls to zero for $x_d \to 1$. For relative photon energies which are smaller than the discontinuity, the intensity spectrum is described by

$$I^c(x, x_d) = \chi(x, x_d) \cdot E_0 \frac{(2\pi)^2}{a^3}|S|^2 e^{-Ag^2} g^2 F(g^2) \tag{5.48}$$

with

$$\chi(x, x_d) = \frac{xQ^2}{1-x}\left(1 + (1-x)^2 - \frac{4x^2Q^2}{1-x}\left(\frac{(1-x)}{xQ} - 1\right)\right), \tag{5.49}$$

$$Q = \frac{1-x_d}{x_d}. \tag{5.50}$$

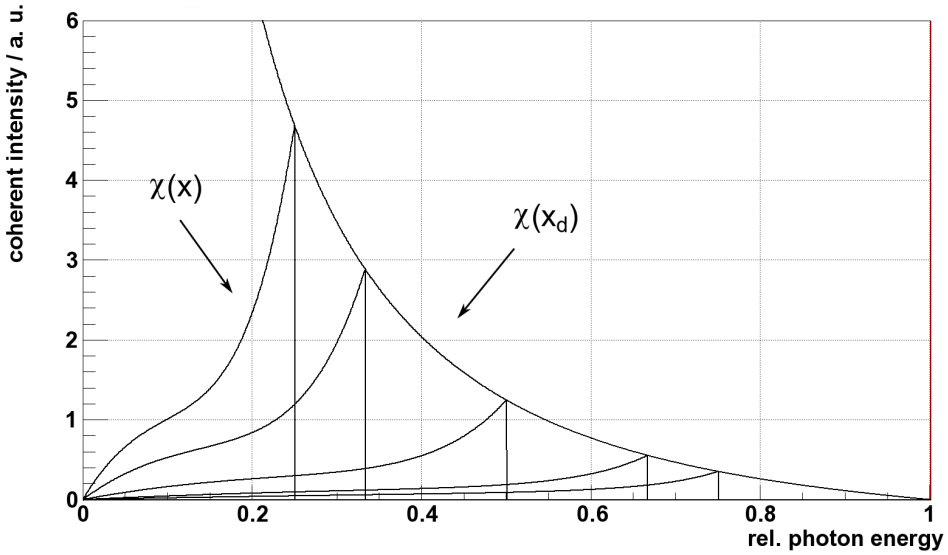

Figure 5.5: $\chi(x)$ (Eq. 5.49) describes the coherent intensity contribution depending on the photon energy for five different orientations of one lattice vector and $\chi(x_d)$ (Eq. 5.47) the maximum intensity contribution in dependence of x_d. The normalisation is arbitrary.

5.3.1 Determination of the Degree of Polarisation

By considering the incoherent contribution, the degree of polarisation can be written as [Tim69]

$$P = \frac{k}{\sigma_0} \cdot \frac{d\sigma^{||} - d\sigma^{\perp}}{d\sigma^{||} + d\sigma^{\perp} + \sigma_{inc}} = 2(1-x)\frac{\Psi_3^c}{I_{inc}} \tag{5.51}$$

with

$$\Psi_3^c = -\frac{1}{2}\frac{(2\pi)^2}{a^3}\delta^3 \sum_{\vec{g}} |S(\vec{g})|^2 e^{-Ag^2} \frac{(1-F(g^2))^2}{g^4} \frac{q_t^2 \cos 2\phi}{q_l^4}. \tag{5.52}$$

Here ϕ denotes the angle between the reference plane and the $(\vec{p_0}, \vec{q})$ plane. Theoretically, the maximum degree of polarisation is obtained for disappearance of the incoherent contribution and if only one lattice vector contributes to the coherent intensity distribution. The degree of polarisation at the discontinuity can be described by

$$P(x_d)_{ideal} = \frac{2(1-x_d)}{(1+(1-x_d)^2)}. \tag{5.53}$$

For smaller photon energies as the discontinuity $x \ll x_d$, the degree of polarisation is given by

$$P(x, x_d)_{ideal} = \frac{2x^2Q^2}{1-x}\left(1 + (1-x)^2 - \frac{4x^2Q^2}{1-x}\left(\frac{1-x}{xQ} - 1\right)\right)^{-1}, \tag{5.54}$$

$$Q = \frac{1-x_d}{x_d} \tag{5.55}$$

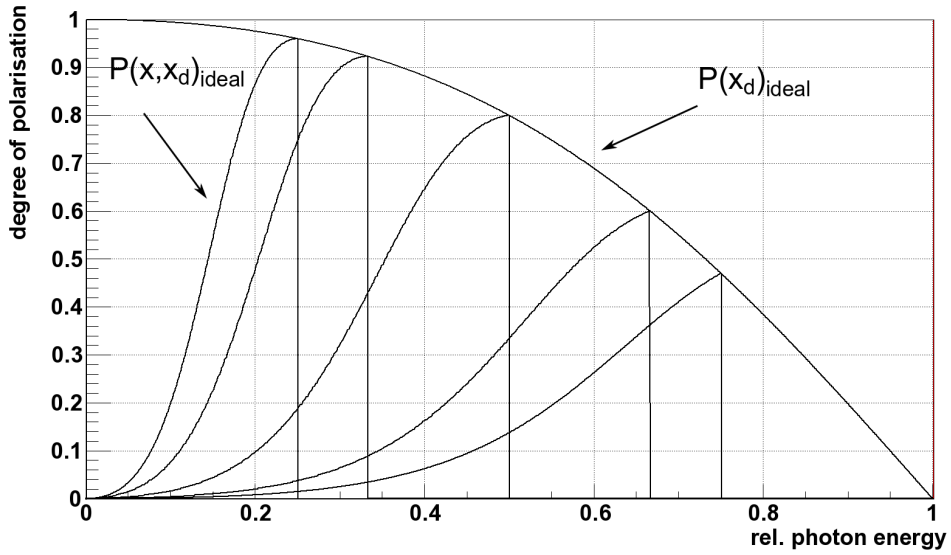

Figure 5.6: $P(x, x_d)_{ideal}$ (Eq. 5.54) describes the degree of polarisation for five different crystal orientations of one reciprocal lattice vector in dependence of the photon energy, while $P(x_d)_{ideal}$ (Eq. 5.53) indicates the maximum degree of polarisation in dependence of the photon energy.

which is demonstrated in figure 5.6. For $x_d \to 0$ the enveloping curve increases asymtotically until full polarisation of the bremsstrahlung photons is achieved, while for $x_d \to 1$ the degree of polarisation drops to zero. Generally, a complete polarisation of the photon beam cannot be accomplished because several reciprocal lattice vectors will lie in the *pancake*, which contribute destructivly to the degree of polarisation. The contribution of the incoherent spectrum, due to thermal excitations, will also decreases the degree of polarisation.

$$P(x, x_d)_{real} = \frac{P(x, x_d)_{ideal}}{1 + \frac{I^{inc}}{I^c}}, \; x \leq x_d. \tag{5.56}$$

5.4 Orientation of the Crystal with Respect to the Electron Beam

The orientation of the crystal with respect to the primary electron beam is significant, as it affects the degree of polarisation. As shown in figure 5.7, the orientation of the crystal can be described with the following angles

$$\theta = (\vec{p_0}, \vec{b_1}) \tag{5.57}$$

$$\alpha = (\vec{b_1}, \vec{b_2})(\vec{p_0}, \vec{b_1}), \tag{5.58}$$

where $\vec{b_1}, \vec{b_2}$ and $\vec{b_3}$ are the crystal axis and $\vec{p_0}$ denotes the momentum of the primary electron beam.

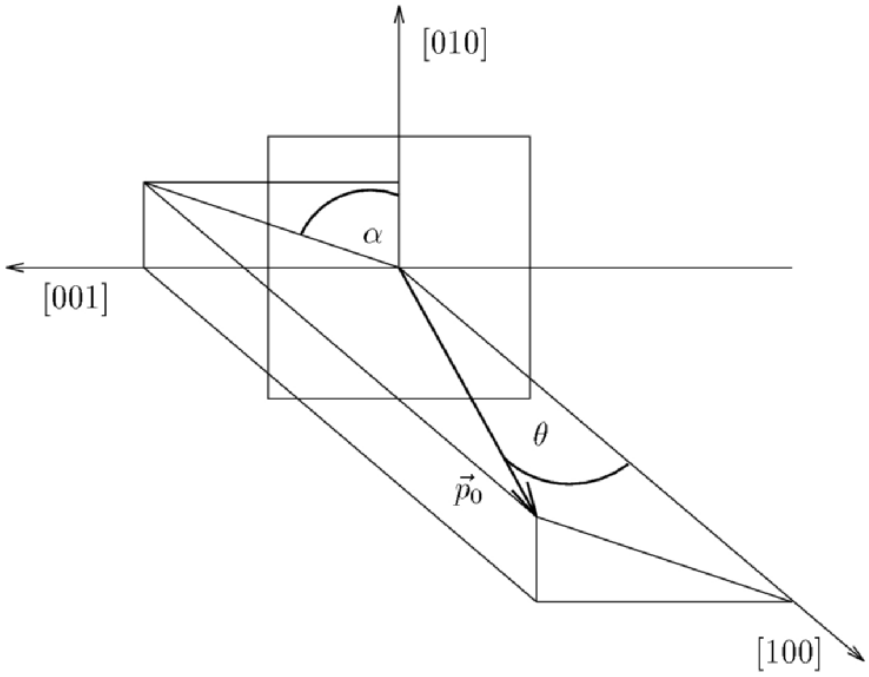

Figure 5.7: Orientation of the crystal in respect to the primary electron beam.

The parameters α and θ can be adjusted by the rotation of the horizontal Φ_H, vertical Φ_V and azimuthal Φ_A angles via the rotation stages of the goniometer.

According to Lohmann [Loh94], the relation between the crystal system $(\vec{b_1}, \vec{b_2}, \vec{b_3})$ and the goniometer system $(\Phi_H, \Phi_V, \Phi_A)$is given by

$$\theta = \arccos(\cos\Phi_H \cos\Phi_V); \tag{5.59}$$

$$\alpha = \arccos\left(\left[-\cos\Phi_A \sin\Phi_H \cos\Phi_V + \sin\Phi_A \sin\Phi_V\right] \left[\sin\theta\right]^{-1}\right), \tag{5.60}$$

Generally three different orientations can be distinguished

1. $\alpha = \theta = 0$**:** For these angles, $\vec{b_1}$ and $\vec{p_0}$ are parallel to each other. In this orientation, several reciprocal lattice vectors lie in the kinematical allowed region and the intensity spectra are called *multipoint spectra*. The first lattice vectors lie on the lower sharp boundary of the *pancake* at $\delta = \frac{4\pi}{a}$. For typical ELSA electron energy$E_0 = 3.2\,\mathrm{GeV}$, this corresponds to $x_d = 0.978$. As shown in figure 5.5 the intensity peaking for this value of x_d is so small that no effective polarisation occurs.

2. $\alpha = 0$ **and** $\theta \ll 1$**:** In this orientation the *pancake* crosses the $\vec{b_2}\vec{b_3}$-plane , as indicated in figure 5.8 on the left. The first, in $\vec{b_3}$ direction extended row of lattice vectors lie at $\delta = \frac{4\pi\theta}{a}$ on the lower sharp limit of the *pancake*. With $E_0 = 3.2\,\mathrm{GeV}$, this corresponds to $x_d = 0.465$. In this region, large intensity peaking is possible, but because the scattering planes can be perpendicular to each other, no effective polarisation can be prepared.

3. $\alpha < 1$ **and** $\theta \ll 1$**:** The selection of one lattice vector can be achieved, by choosing $\alpha \neq 0$. Intensity spectra which are caused by one lattice vector are called *one point spectra*. In this case it is possible to rotate the crystal such, that for example only the $[02\bar{2}]$ vector lies on the lower boundary of the *pancake*. The intensity peaking is not as high as for the *multipoint spectra*, but due to the fact, that only one lattice vector contributes to the intensity spectrum, a high degree of polarisation can be achieved.

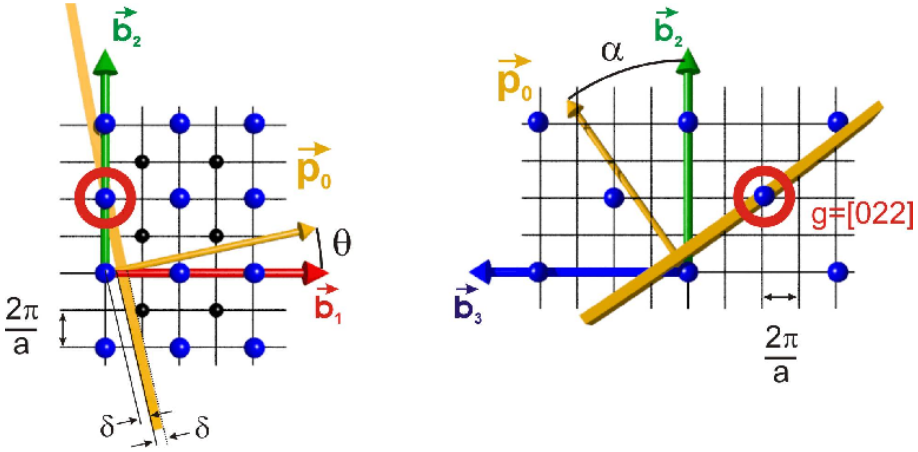

Figure 5.8: Orientation of the crystal in respect to the electron beam and therefore to the *pancake* [Els07]. Here $\vec{b}_1$, $\vec{b}_2$ and $\vec{b}_3$ denote the unit vectors of the reciprocal lattice, $\vec{p}$ is the momentum of the incident electron beam, a the lattice constant, the points represents reciprocal lattice vectors and the yellow stripes describes the pancake which is perpendicular to the electron momentum. Left: For $\theta \ll 1$ and $\alpha = 0$, the row of lattice vectors in $\vec{b}_3$ direction contributes to a multipoint spectrum. Right: For $\theta \ll 1$ and $\alpha \neq 0$, the selection of one lattice vector is possible.

6 Consideration of Experimental Influences

For the calculation of the intensity spectra, an ideal primary electron beam was assumed until now. In general, the electron beam will diverge and in addition, by travelling through the radiator, the electron beam will undergo multiple scattering. These effects lead to an effective deviation of the ideal primary electron momentum vector and therefore to different electron beam angles with respect to the crystal lattice. This results in a smeared out discontinuity and in consequence a decrease of the degree of polarisation.

According to equation 5.56 it is possible to increase the degree of polarisation by reducing the incoherent intensity contribution. Because the angular distribution of incoherent bremsstrahlung photons (Eq. 6.4) is much broader than for coherent (Eq. 6.1) ones, a collimator reduces the incoherent contribution more effectively and an increase in the degree of polarisation can be achieved. Due to the different angular distributions of the coherent and the incoherent part, the consideration of collimation in the calculations has to be treated differently for each intensity contribution.

For a realistic description of measured intensity spectra, it is necessary to consider these beam properties and the collimation.

6.1 Collimation of the Bremsstrahlung Photon Beam

Photons produced in the coherent bremsstrahlung process are emitted in extreme forward directions. The angular distribution for the coherent intensity distribution, according to [Nat03], is given by

$$u_k = \sqrt{\frac{g_l}{\delta} - 1} = \sqrt{\frac{1-x}{x} \cdot \frac{x_d}{1-x_d} - 1}. \tag{6.1}$$

Here, δ denotes the lower limit of the pancake, given by equation 5.9, $x = k/E_0$ the relative photon energy, x_d the photon energy at the discontinuity given by equation 5.16 and g_l the longitudinal component of the reciprocal lattice vector. Equation 6.1 shows, that the photon opening angle increases with decreasing photon energy. A collimator placed in the beam axis, defines an upper limit for the photon opening angle $u_c = \theta_c E_0$. The corresponding minimum photon energy is given by

$$x_c = \frac{x_d}{1 + u_c^2(1 + x_d)}. \tag{6.2}$$

In this case for coherent bremsstrahlung an upper sharp limit in the *pancake* area, due to the collimator, can be realised.

According to [Bet34], the angular distribution of the incoherent intensity spectrum is given as

$$d^3\sigma^{incoh} \approx d\sigma^{incoh} \frac{u_k du_k d\omega}{(1 + u_k^2)^2} \quad \text{with} \quad u_k = \theta_k E_0. \tag{6.3}$$

Here θ_k describes the photon opening angle, ω the azimuthal emission angle and E_0 the primary electron energy. According to [Ram98], a computational fit of 6.3 leads to

$$d^3\sigma^{incoh} \approx d\sigma^{incoh} \cdot \frac{1}{\pi(A_1 s_1^2 + A_2 s_2^2)} \sum_{i=1}^{2} A_i \exp(-u_k^2/s_i^2) u_k du_k d\omega \tag{6.4}$$

With $A_1 = 0.7$, $A_2 = 0.3$, $s_1 = 0.637$ and $s_2 = 1.41$. To describe the collimation in the incoherent part, the intensity contribution has to be multiplied by a reduction factor. The reduction factor [Tim69] which is given by equation 6.5 is determined by the ratio of the collimated and the uncollimated intensity distribution.

$$f_c = \frac{\int_0^{u_c} d^3\sigma^{incoh}}{\int_0^{\infty} d^3\sigma^{incoh}} = \frac{u_c^2}{1 + u_c^2}. \tag{6.5}$$

6.2 Primary electron beam divergence and multiple scattering

The accelerated electron beam is not ideally parallel. Due to the repelling Coulomb force, the electrons diverge from their ideal trajectory which leads to different momenta $\vec{p_0}$ and therefore to different crystal angles θ and α (Eq. 5.57) with respect to the primary electron beam. Before the electron beam impinges on the radiator it is focused by a quadrupol magnet in one plane. Perpendicular to this plane the beam is defocussed which leads to an elliptical shape of the electron beam. Hence, the electron beam divergence is approximated by a two dimensional Gaussian function

$$BD(\Delta_{dx}, \Delta_{dy}) = \frac{1}{2\pi\sigma_{dx}\sigma_{dy}} \exp\left(-\frac{\Delta_{dx}^2}{\sigma_{dx}^2} - \frac{\Delta_{dy}^2}{\sigma_{dy}^2}\right). \tag{6.6}$$

Here, Δ_{dx} and Δ_{dy} are the angles which denote the transversal deviations of the primary electron momentum. σ_{dx} and σ_{dy} are the corresponding standard deviations.

Due to the fact, that the radiators have a finite thickness, multiple scattering of the electrons in the radiator has to take into account. This effect causes, like the beam divergence a smearing of the discontinuity. According to Moliére [Mol48], the scattering angle Θ_{mol} distribution can be represented by a series expansion as follows

$$f(\Theta_{mol})\Theta_{mol}d\Theta_{mol} = \theta d\theta \left[f^{(0)}(\theta) + B^{-1}f^{(1)}(\theta) + B^{-2}f^{(2)}(\theta) + ...\right] \tag{6.7}$$

$$\text{with} \quad \theta = \Theta_{mol}/(\chi_c\sqrt{B}) \tag{6.8}$$

$$\text{and} \quad \chi_c = 0.3965 \cdot \frac{Z(Z+1)}{p\beta}\sqrt{\frac{\rho s}{A}}. \tag{6.9}$$

Here Z denotes the atomic number, p the electron momentum, β electron velocity, ρ the density of the material, s the distance through the crystal and A the atomic mass. B and the $f^{(i)}$ functions can be looked up in [Mol48]. For small scattering angles Θ_{mol}, the function $f^{(0)}$ corresponds to a Gaussian function with $f^{(0)} = 2e^{-\theta^2}$. For a more precise calculation at least the next two orders of the series have to be considered. A more accurate approximation of the scattering angle distribution

which also corresponds to a Gaussian function is given in [Hig75]. The standard deviation, that is used in the further calculations, is given by [Eid04]

$$\sigma_{ms}(s) = \frac{13.6MeV}{p\beta}\sqrt{\frac{s}{X_0}}\left[1 + 0.038\ln\left(\frac{s}{X_0}\right)\right]. \tag{6.10}$$

Here s denotes the path length in the crystal and X_0 the radiation length. The parameters p and β are defined as before.

To simplify the computation of multiple scattering, the following approximation is used for the standard deviation

$$\bar{\sigma}_{ms} = \frac{1}{d}\int_0^d \sigma_{ms}(s)\mathrm{d}s \tag{6.11}$$

where d denotes the crystal thickness and s the path length in the crystal. The Gaussian function that describes multiple scattering can be written as

$$VS(\Delta_{ms}) = \frac{1}{2\pi\bar{\sigma}_{ms}^2}\exp\left(-\frac{\Delta_{ms}^2}{\bar{\sigma}_{ms}^2}\right). \tag{6.12}$$

In this case Δ_{ms} is the angle, which indicates the transversal deviations of the primary electron momentum due to multiple scattering, while $\bar{\sigma}_{ms}$ specifies the mean standard deviation from above.

According to [Ram98] convolution of the distributions 6.6 and 6.12, yields to an overall electron angular distribution of the form

$$ED(\Delta_{ex}, \Delta_{ey}) = \frac{1}{2\pi\sigma_1\sigma_2}\exp\left(-\frac{\Delta_{ex}^2}{\sigma_1^2} - \frac{\Delta_{ey}^2}{\sigma_2^2}\right) \tag{6.13}$$

with transverse widths

$$\sigma_{1/2}^2 = \sigma_{dx/dy}^2 + \frac{\bar{\sigma}_{ms}^2}{2}. \tag{6.14}$$

To calculate the resulting coherent intensity distribution (Eq. 6.16), an integration over all possible directions of the electrons momentum vector has to be performed. Due to the deviation of the electrons direction, new angles with respect to the lattice of the crystal have to be calculated and used for the determination of the intenisty. Therefore, the goniometer angles Φ_H and Φ_V, which were introduced in chapter 5 are extended by the transverse deviation of the electrons momentum

$$\Phi_H^{new} = \Phi_H + \Delta_{ex} \quad \text{and} \quad \Phi_V^{new} = \Phi_V + \Delta_{ey} \tag{6.15}$$

and converted by equation 5.59 into new crystal angles α^{new} and θ^{new}. The intensity is then weighted by the probability that an electron impinges on the crystal with transverse deviation Δ_{ex} and Δ_{ey}. After this integration, the intensity spectrum is divided by the effective electron beam divergence distribution. The coherent intensity contribution considering beam divergence and multiple scattering is given by

$$I^{coh}_{new} = \frac{\int \mathrm{d}\Delta_{ex}\mathrm{d}\Delta_{ey}\ ED(\Delta_{ex},\Delta_{ey})\ I^{coh}(\alpha^{new},\theta^{new})}{\int \mathrm{d}x\mathrm{d}y\ ED(\Delta_{ex},\Delta_{ey})}. \tag{6.16}$$

Due to the rotational symmetry of incoherent bremsstrahlung, beam divergence and multiple scattering have no noticeable effect on the incoherent intensity as long as the photon beam is not collimated.

6.3 Collimation and Effective Beam Divergence

In the first paragraph of this chapter, an ideal electron beam was assumed when taking the collimation into account. By considering electron beam divergence and multiple scattering the consideration of the collimation in the incoherent intensity contribution has to be changed, while the collimation in the coherent intensity contribution is still considered by equation 6.2. According to [Ram98] the reduction factor f_c has to be modified. Here 6.4 and 6.13 have to be convulated, which results in an effective incoherent angular distribution

$$AD(\Delta_{ax},\Delta_{ay}) = \frac{1}{4\pi(A_1 s_1^2 + A_2 s_2^2)} \sum_{i=1}^{2} A_i \frac{s_i^2}{\sigma_{i1}\sigma_{i2}} \exp\left(-\frac{\Delta_{ax}^2}{2\sigma_{i1}^2} - \frac{\Delta_{ay}^2}{2\sigma_{i2}^2}\right) \tag{6.17}$$

with widths

$$\sigma_{ij}^2 = \sigma_i^2 + \frac{s_j^2}{2}, \quad i,j = 1,2. \tag{6.18}$$

The modified reduction factor is then given by

$$f_c = \frac{\int_{r_\gamma \le R} AD(\Delta_{ax},\Delta_{ay}) d\Delta_{ax} d\Delta_{ay}}{\int AD(\Delta_{ax},\Delta_{ay}) d\Delta_{ax} d\Delta_{ay}}. \tag{6.19}$$

R denotes the radius of the collimator, r_γ defines the position of the bremsstrahlung photon in the collimator and is given by

$$r_\gamma = \frac{L}{E_0}\sqrt{\Delta_{ax}^2 + \Delta_{ay}^2} \tag{6.20}$$

Here L indicates the distance of the collimator from the radiator and E_0 the primary electron energy.

In chapter 5, the incoherent and the coherent bremsstrahlung process were described assuming an ideal electron beam. Generally, the electron beam diverges and undergoes multiple scattering by travelling through a radiator. To increase the degree of polarisation, the photon beam is collimated. In order to describe incoherent and coherent intensity spectra, these experimental conditions have to be considered in the calculations for the coherent and incoherent intensity contributions. The methods for these considerations were presented in this chapter. For the describtion of measured intensity spectra a program (COBRIS) was developed which uses the calculations presented in chapter 5 and 6. This program and the effects of the experimental conditions on the coherent and incoherent intensity spectra will be presented in the next chapter.

7 Calculation of Bremsstrahlung Intensity Spectra (COBRIS)

As explained in chapter 5, the cross section for bremsstrahlung in a crystal can be written as the sum of the coherent and the incoherent cross sections. To accentuate the intensity peaking of the coherent bremsstrahlung photons, the intensity spectrum of a crystal is divided by the incoherent spectrum. Because it is not possible to measure the incoherent contribution in a crystal separately, an intensity spectrum of an amorphous radiator like copper is used for the normalisation of the coherent intensity spectrum. This is illustrated in figure 7.1.

To describe the relative intensity spectrum and to determine the degree of polarisation, the ANB program [Nat03] is currently used at the Crystal Barrel experiment. The incoherent intensity contribution calculated by the ANB program has to be scaled by 30% for an adequate description of relative intensity spectra. In addition, the consideration of collimation does not work correctly. Although the consideration increases the degree of polarisation, however, decreases the degree of polarisation if the radius of the collimator is further reduced. Due to this circumstances a new program was written, which is mainly based on papers of U.Timm [Tim69], D. Lohman [Loh94] and F.Rambo [Ram98]. The program is described in this chapter.

7.1 Introduction of COBRIS

COBRIS is written in C++, allowing a modular design which results in a clear description of the written code and simplifies adding new elements. To commit easily the start parameters to COBRIS and to compare directly the calculated intensity spectra with measured data, a user-friendly graphical interface is written (s. figure 7.2). For the graphical user interface, Qt 4.6.3 of Nokia[1] is used. The

[1] qt.nokia.com

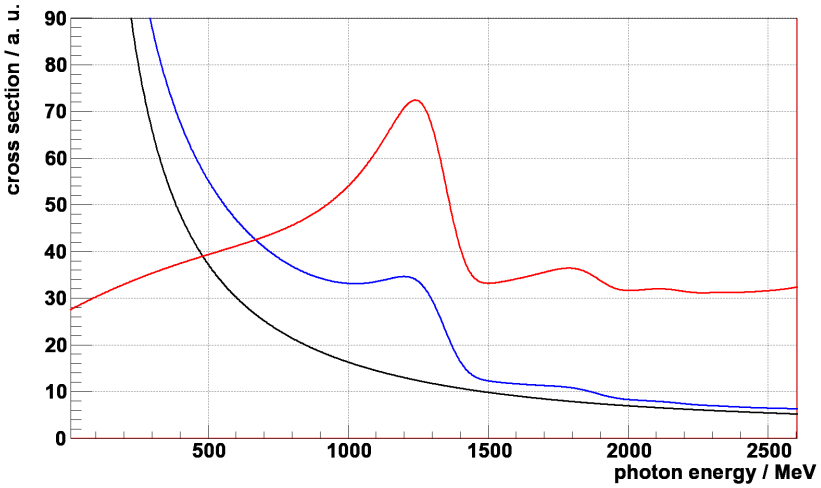

Figure 7.1: Calculated bremsstrahlung intensity spectra. In black, an incoherent spectrum for copper, in blue a coherent spectrum for diamond. The relative spectrum of the two spectra is given by the red curve.

graphical presentation and is performed by ROOT[2] and implementet by using the QTROOT plugin[3].

Start parameters to compute the bremsstrahlung intensity spectra are classified in electron beam, radiator and collimator parameters, which are listed in the following table. In a first step, COBRIS computes, for the alternatively handed over

Electron beam	Radiator	Collimator
Energy E_0	Crystal thickness d	Distance to radiator L
Divergence σ_{dx}	Temperature T	Radius r
Divergence σ_{dy}	gonimeter angle Φ_V	Length l
	gonimeter angle Φ_H	
	gonimeter angle Φ_A	
	Atomic number of copper Z_{amo}	
	Atomic number of Diamond Z_{cry}	

Table 7.1: Input parameters for the calculation of bremsstrahlung spectra.

goniometer or crystal angles, the maximum intensity contribution of about 900 lattice vectors and sorts them. The user now chooses the lattice vectors which he wants to consider in the calculation. After doing this, COBRIS calculates successively the coherent and incoherent intensity contribution of the crystal and the

[2]http://root.cern.ch
[3]http://root.bnl.gov

incoherent intensity contribution of the amorphous radiator. Finally this data is stored in a text file and root file and visulalised by COBRIS.

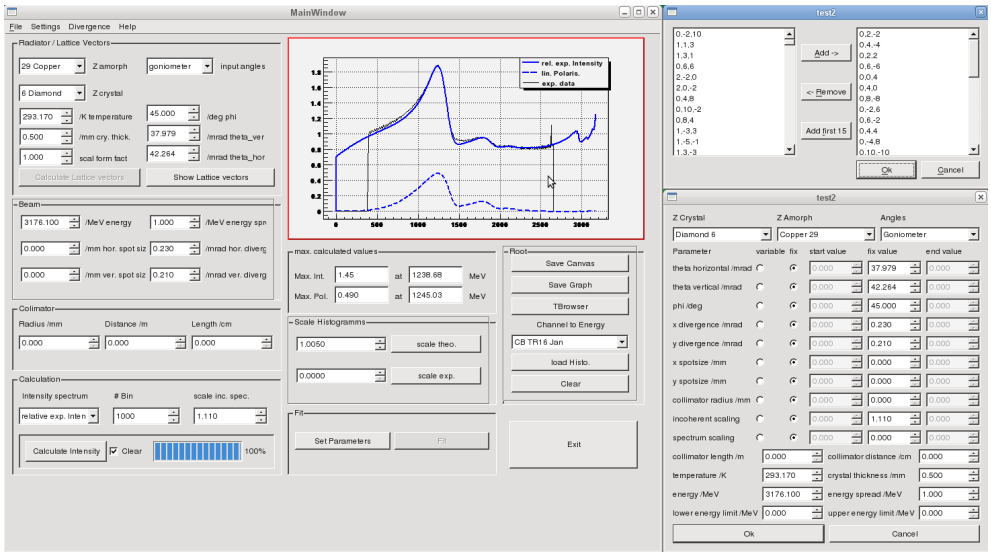

Figure 7.2: Graphical user interface of COBRIS

7.2 Determination of Intensity Spectra for an Ideal Electron Beam

The computed intensity spectra for typical primary electron energies at ELSA of $E_0 = 3200\,\mathrm{MeV}$, a diamond crystal with $Z_{cry} = 6$ and copper with $Z_{amo} = 29$ as radiators and goniometer angles with $\Phi_V = 37.979\,\mathrm{mrad}$ and $\Phi_V = 42.264\,\mathrm{mrad}$ corresponding to crystal angles $\theta = 56.813\,\mathrm{mrad}$ and $\alpha = 0.731\,\mathrm{rad}$ is shown in figure 7.3. In this case, beam divergence, multiple scattering and collimation are not included. The intensity peakings with the sharp edges at the discontinuities, for the contributions of the [022], [044], [066] and [088] lattice vectors can be clearly seen. With these parameters a degree of polarisation of almost 60 % is achieved. In the next paragraphs the effects of collimation, beam divergence and multiple scattering are illustrated.

7.3 Collimation of the Bremsstrahlung Photon Beam

A collimator affects the coherent and the incoherent contribution in different ways. The influence of the collimator is introduced in chapter 6 and used for the de-

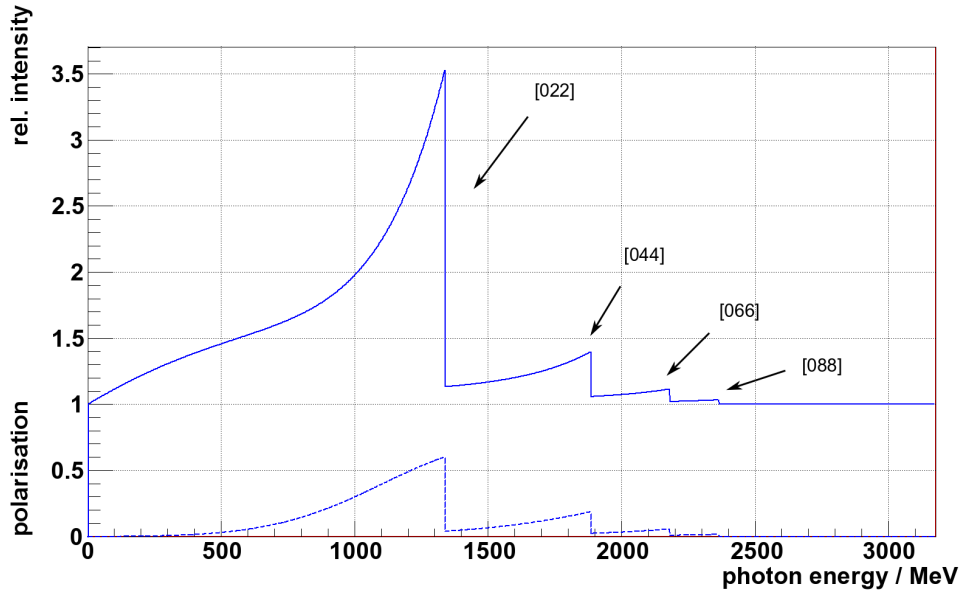

Figure 7.3: Calculated relative intensity spectrum for an ideal electron beam. The blue curve describes the relative intensity spectrum, while the blue dotted line describes the degree of polarisation. Coherent intensity contributions of the [022], [044], [066] and [088] lattice vectors can be seen.

scription of collimated intensity spectra. Choosing the collimator parameters as $L = 3.26\,\mathrm{m}$, $r = 1.5\,\mathrm{mm}$ and $l = 24\,\mathrm{mm}$, the resulting incoherent intensity spectrum is shown in figure 7.4. The maximum opening angle is given by $u_c = r/(L+l)$, which due to equation 6.5 leads to a reduction factor of $f_c = 0.76$. The whole incoherent intensity contribution is reduced by this factor.

In contrast, the coherent intensity contribution depends on the photon energy. Reducing the maximum opening angle by a collimator is equivalent to a minimum photon energy, which has to be reached to pass the collimator. The minimum photon energy is given by equation 6.2. The effect of collimation in the coherent intensity contribution is noticeable by hard edges in the relative intensity spectrum, demonstrated in figure 7.5. The edge at about 250 MeV corresponds to the intensity contribution of the [022] lattice vector. A second one can be seen at energies of 490 MeV, corresponding to the [044] lattice vector. In this case the overlap of the different lattice vector contributions can be seen clearly. The corresponding cut of the [066] lattice vector lies at energies of about 690 MeV. For the calculations, the same parameters as for the uncollimated spectrum were used. In both cases, the influence of beam divergence and multiple scatterin was not included. Beam divergence and multiple scattering will be considered in the next section.

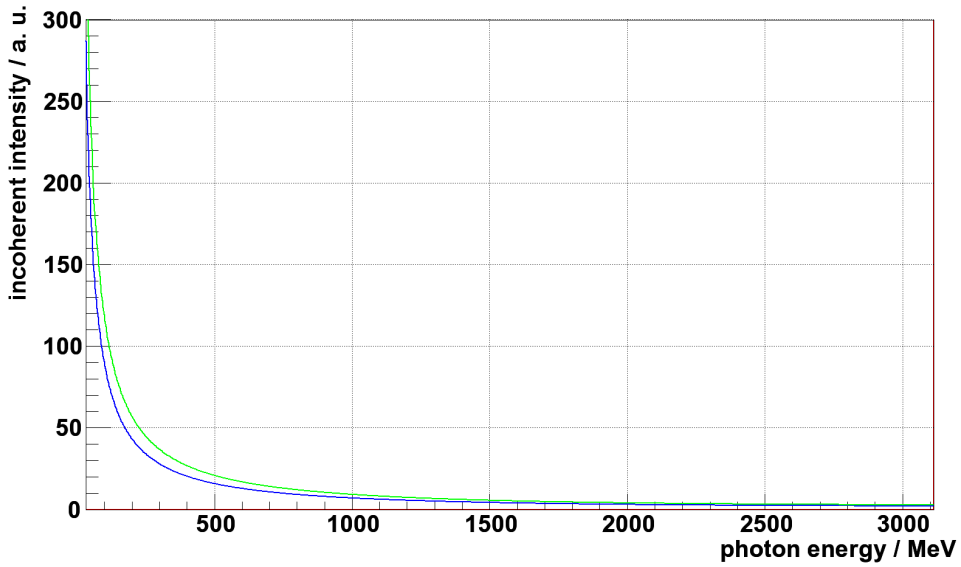

Figure 7.4: Influence of the collimator on an incoherent intensity spectrum. The green line shows the uncollimated incoherent intensity contribution, while the blue describes the collimated one, which is scaled by the reduction factor f_c (Eq. 6.5)

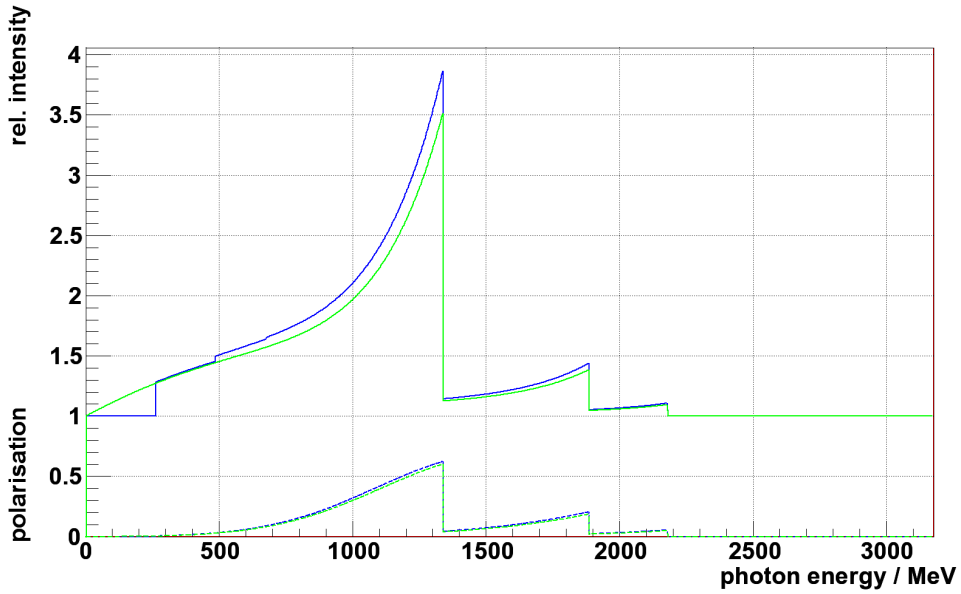

Figure 7.5: Influence of the collimator on a relative intensity spectrum. The green line shows the uncollimated relative intensity contribution. The blue curve illustrates the increase of polarisation by using a collimator. The two steps indicate the sharp upper limit in the kinematical allowed region due to the collimator for the [022], [044] and the [066] lattice vector

7.4 Beam Divergence and Multiple Scattering

Due to multiple scattering and beam divergence, the electrons direction relative to the crystal lattice varies. This causes the discontinuity to change into a smoothly varying peak. Figure 7.6 shows the effect of beam divergence and multiple scattering on a uncollimated relative intensity spectrum. With paramaters for beam divergence $\sigma_{dx} = 0.23\,\text{mrad}$, $\sigma_{dy} = 0.21\,\text{mrad}$ and a crystal thickness of $500\,\mu\text{m}$, the effective standard deviations are computed from equations 6.10, 6.11 and 6.14 to $\sigma = 0.27\,\text{mrad}$ and $\sigma_2 = 0.25\,\text{mrad}$. The discontinuity is smoothed by considering beam divergence and multiple scattering. The direct consequence is a decrease in the maximum degree of polarisation.

If collimation also is considered, the incoherent spectrum is stronger reduced as without considering beam divergence (s. figure 7.7). With divergence a further decrease in the incoherent intensity spectrum is expected, due to the deviation of the electrons from their forward trajectory. In the coherent part, the limitations caused by the collimator are smoothed like the edges at the discontinuities. Due to the lower incoherent intensity contribution, the coherent insensity peaking increases which leads to a higher degree of polarisation. The consideration of a collimator on a relative intensity spectrum which is affected by beam divergence and multiple scattering is illustrated in figure 7.8. In this case, the same parameters as for the uncollimated spectrum were used and complemented by the parameters for beam divergence, multiple scattering and collimation.

In this chapter the effects of beam divergence, multiple scattering and collimation were presented. The consideration of beam divergence and multiple scattering leads to a smoothed discontinuity of the coherent edges in the relative intensity spectra and therefore a decrease of the degree of polarisation. Using a collimator allows an increase of the degree of polarisation by reducing the incoherent intensity contribution. The next step is to compare the calculations done by COBRIS with measured data. Therefore Crystal Barrel data were used. The results are presented in the next chapter.

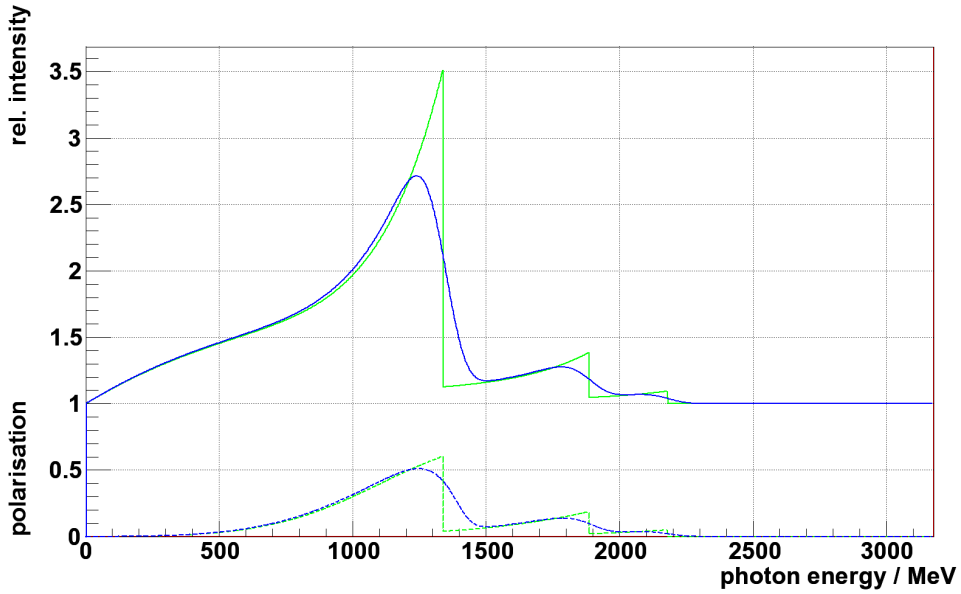

Figure 7.6: Consideration of beam divergence and multiple scattering without collimation. In green a relative intensity spectrum for an ideal electron beam. In blue with experimental conditions, by using the parameters $\sigma_{dx} = 0.23\,\text{mrad}$ and $\sigma_{dx} = 0.21\,\text{mrad}$ for beam divergence and a crystal thickness of $500\,\mu\text{m}$.

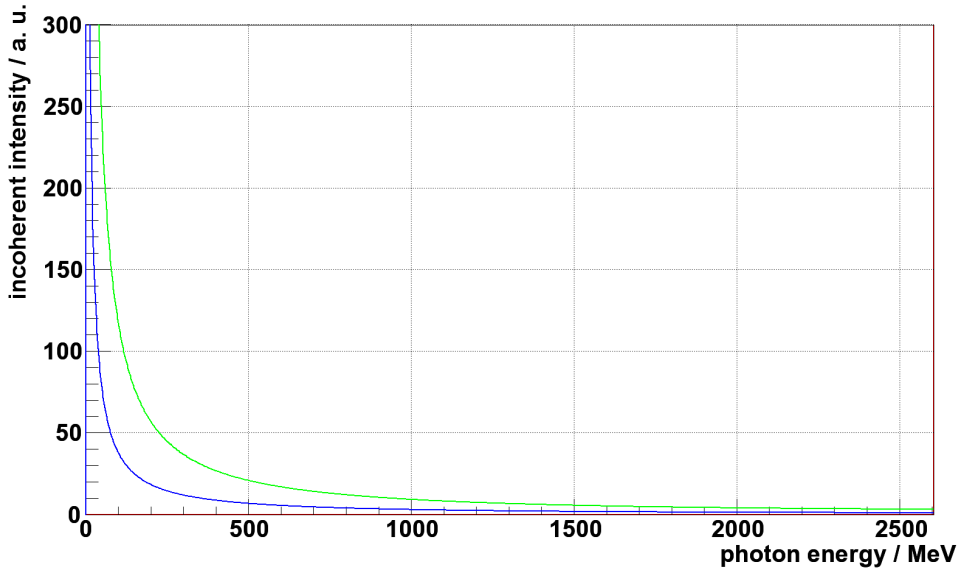

Figure 7.7: Influence of beam divergence, multiple scattering and collimation on an incoherent intensity spectrum. The green line shows the uncollimated incoherent intensity contribution, while the blue describes the collimated one. Due to beam divergence and multiple scattering the incoherent intensity contribution is more reduced.

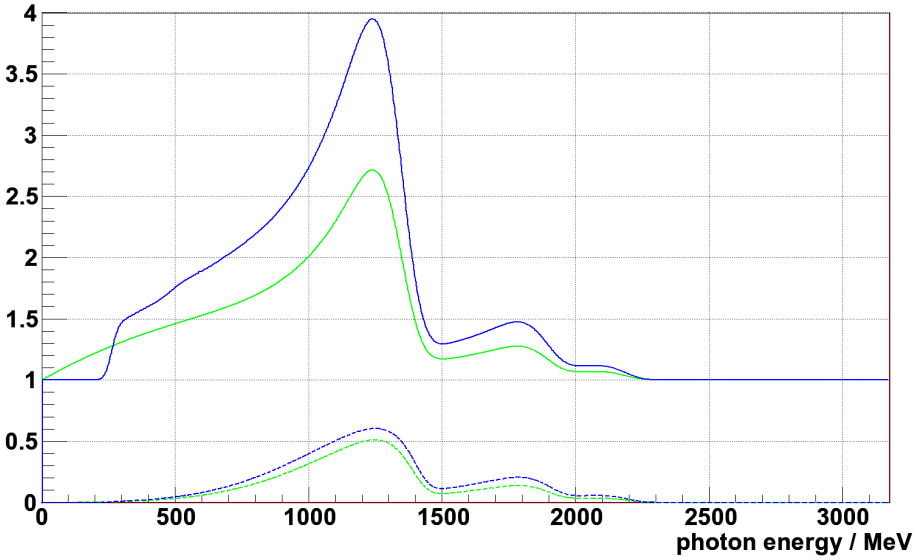

Figure 7.8: Influence of beam divergence, multiple scattering and collimation on a relative intensity spectrum. The green line shows the uncollimated relative intensity contribution, the blue line collimated relative intensity contribution. The discontinuities due to the collimator are smoothed due to the beam divergence and multiple scattering

8 Comparision with Measured Data from Crystal Barrel

For the determination of the degree of polarisation the software COBRIS was developed. For a satisfactory description of measured data, beam divergence, multiple scattering and collimation of the photon beam must be considered in the calculations. The calculations to consider the experimental conditions were presented in chapter 6. To compare the calculations done by COBRIS with measured relative uncollimated and collimated intensity spectra, data from the CB experiment were used. The results will be presented in this chapter.

8.1 Measured Crystal Barrel Data

For the comparison with COBRIS uncollimated and collimated measured spectra were used. As mentioned in chapter 3, it is possible to determine the bremsstrahlung photon energy with a tagging system. Electrons which have produced bremsstrahlung photons are momentum analysed by a dipole magnet and bended into a hodoscope. Depending on the energy of the scattered electrons, the electrons are registrated by different scintillators. To get the photon intensity spectrum, the channel number has to be converted into the corresponding photon energy [FP09] by a so called energy calibration. A typical tagger spectrum for both cases is shown in figure 8.1.

It is possible to receive a collimated intensity spectrum in addition with the coincidence between the tagger system and a gamma intensity monitor (GIM). The GIM is placed in the photon beam line at the end of the experiment and counts the incoming photons which have passed the collimator.

For measurements with the Crystal Barrel setup, electrons with an energy of $3176,1$ MeV were irradiated on a diamond crystal with a thickness of $0.5\,\mathrm{mm}$ and on copper radiators. Due to statistics the coherent intensity spectrum was accumulated from measurements over several days. During this time the angle of the primary electron beam on the crystal may change due to slight changes of the optic of the

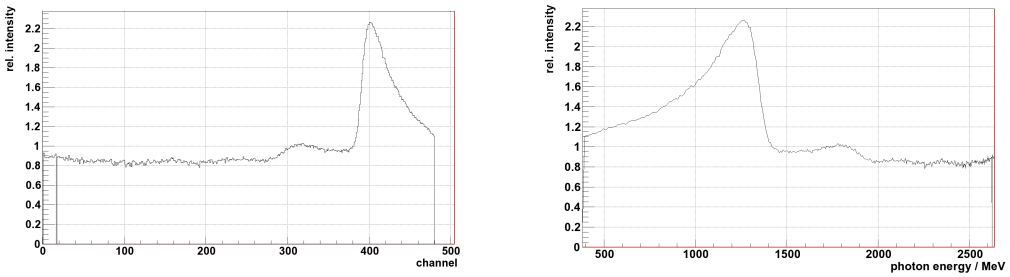

Figure 8.1: Measured tagging spectrum. **Left**: relative measured electron spectrum. **Right**: relative converted intensity spectrum.

beam line. The deviation of the reference electron trajectory leads to a shift of the discontinuity in the intensity spectrum (Eq. 5.16). In order to avoid the deviations of the discontinuity a reference spectrum was taken and compared continously with the measurements [Els07]. If the measured intensity spectrum differs to much from the refenrence spectrum the orientation of the crystal with respect to the electron beam or the position of the primary electron beam was corrected. Due the stability of the beam, statistics of individual measurement periods of over typically two days were summed and used for the comparison.

8.2 Comparision of COBRIS with an Uncollimated Spectrum

To verify the approximation of beam divergence and multiple scattering by an effective Gausian function (Eq. 6.13), an uncollimated measured spectrum for the comparison is used first. Figure 8.2 shows the comparison of a calculated and measured relative intensity spectrum. The gonimeter angles are $\Phi_{hor} = 42.264\,\text{mrad}$ and $\Phi_{ver} = 37.979\,\text{mrad}$, which correpond to the following crystal angles $\theta = 56.813\,\text{mrad}$ and $\alpha = 0.731\,\text{rad}$ with respect to the primary electron beam. The standard deviations for the consideration of beam divergence are not known exactly. Simulations showed that the beam divergence are of the order of $\sigma \sim 0.1\,\text{mrad}$ [Els07]. For the comparison the beam divergence has been adjusted to the spectrum and is given by $\sigma_{dx} = 0.23\,\text{mrad}$ and $\sigma_{dy} = 0.21\,\text{mrad}$. In total, the first 30 reciprocal lattice vectors with the largest intensity contributions are considered in the calculations which is satisfactory, because calculations with more lattice vectors showed no significant change in the intensity spectra. The temperature of the

crystal was assumed to be 293 K. The data were normalised in the high energy range.

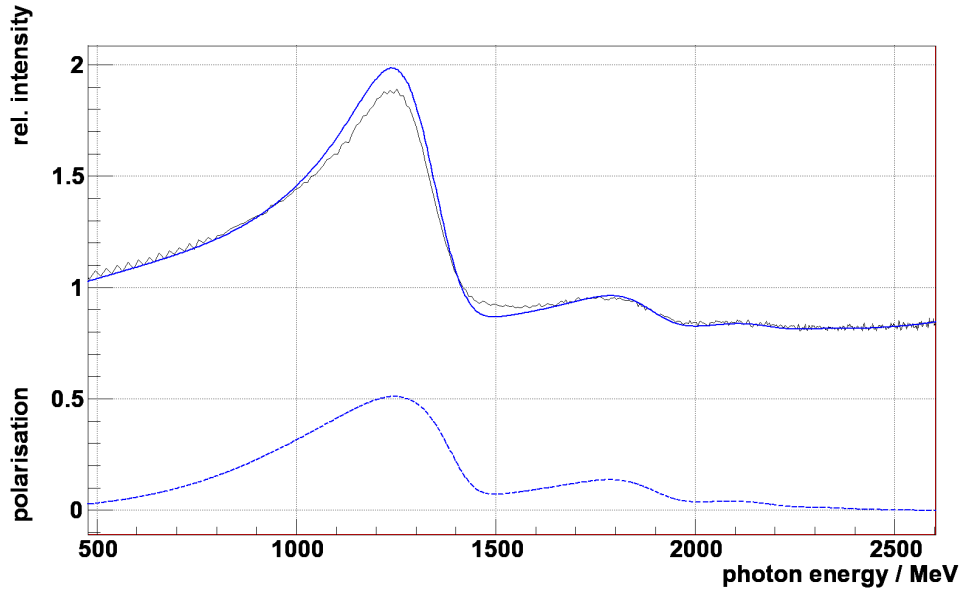

Figure 8.2: Comparision of COBRIS with a measured uncollimated relative intensity spectrum. The measured data is given by the black line, while the blue line indicates the theoretical spectrum. The dotted blue line describes the resulting degree of polarisation.

The theory differs significantly from the measured data in the intensity peaks. This indicates an underestimation of the incoherent intensity contribution. A better description can be found if the incoherent intensity spectrum is scaled by about 10%. A possible reason for the scaling is the uncertainty of the used atomic form factor. The same description of the data can be realised if the atomic form factor is scaled by about 10% (Eq. 5.29)

$$F(q) = \frac{1}{q^4}(1 - F'(q) \cdot x_{sca})^2 \quad \text{with} \quad x_{sca} = 1.10. \tag{8.1}$$

The result is illustrated in figure 8.3

If the parametrisation of the atomic form factor given by [Sch51] with $C = 111$ instead of [MFO92], a scaling factor of approx 17% for the incoherent intensity sepctrum or 22% for the atomic form factor is necessary. The deviations of the scaling factors are of the same order of magnitude as the difference between the parametrisations of the atomic form factors, which are shown in Figure 5.4. This indicates an inadequate description of the atomic form factor, which could cause the

deviations in the discription. The ANB program, written by F.A. Natter [Nat03]

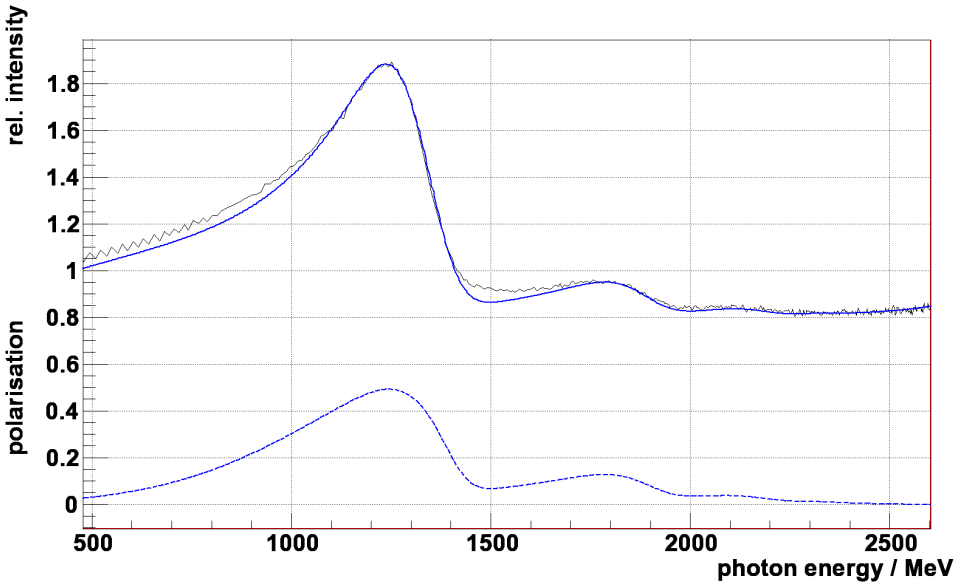

Figure 8.3: Comparision of COBRIS with scaled incoherent intensity contribution with a measured uncollimated relative intensity spectrum. The measured data is given by the black line, while the blue line indicates the simulated spectrum. The dotted blue line describes the degree of polarisation.

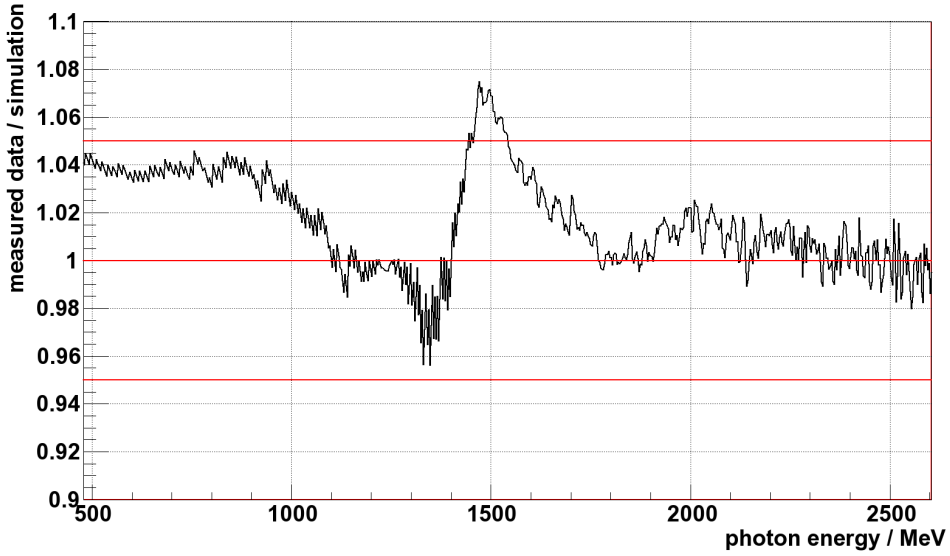

Figure 8.4: Relative deviation of an uncollimated measured intensity spectrum to the simulation (COBRIS). The relative deviation is given by the black curve, while the red lines donate the region with deviations of ±5% and 0%.

at the University of Tübingen is currently a standard tool for the calculation of the degree of polarisation for experiments at the Electron Strecher Accelerator in Bonn, at the Thomas Jefferson National Accelerator Facility (JLAB) in Virginia and at the Mainzer Microtron (MAMI). Experiments at JLAB and ELSA which use electron beams of $E_0 > 3\,\mathrm{GeV}$ need also a scaling factor for the description of the incoherent intensity contribution. According to ([Gor04],[Mel05]) a scaling factor of about ≈ 1.5 is needed to describe measured data of the CLAS[1] experiment with the ANB program. Also the data of the CB experiment are in agreement with the ANB code by using a scaling factor of ≈ 1.35 [Els07]. With the description of the data by the COBRIS calculation the maximum degree of polarisation in this intensity spectrum is reached at $E_\gamma \approx 1245\,\mathrm{MeV}$ with 49.2%. Figure 8.4 shows the relative deviations of the measured intensity spectrum to the simulation. The peaks in the intensity spectrum can be described very well. A maximal relative deviation of 8% exists at an energy of approximately $E_\gamma = 1500\,\mathrm{MeV}$, while the rest of the simulation differs maximal up to about 4%. In comparision to the unscaled relative intensity spectrum the degree of polarisation differs at the energy $E_\gamma \approx 1245\,\mathrm{MeV}$ by nearly 4% relative which is shown in figure 8.5. The largest deviation of almost 9,5% is reached at high energies where no effective polarisation exists. By computing

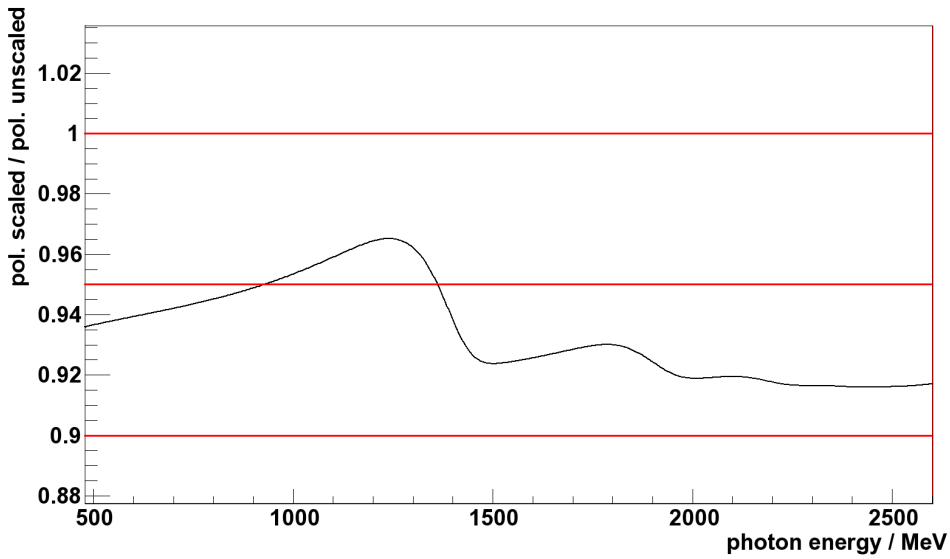

Figure 8.5: Relative deviation of the degree of polarisation. The relative deviation is given by the black curve, while the red lines donate the region with deviations of 0%, 5% and 10%.

[1] **C**EBAF **L**arge **A**cceptance **S**pectrometer

the relative intensity spectrum it is possible that deviations in the incoherent and coherent intensity spectra cancel out each other. Hence it has to be proofed if these sepctra can also be described by the simulation. Figure 8.6 and 8.7 show the comparison of the incoherent and coherent intensity spectrum with the simulation. The measured intensity spectra are not efficiency corrected which explains the structures in the intensity spectra especially in the energy range of $E_\gamma = 630\,\text{MeV}$ - 800 MeV. Therefore the simulations are scaled such that the measured intensity spectra are described most accurately in the energy region of about $E_\gamma = 1000\,\text{Mev}$ - 2100 MeV. Exept for the inefficency effects, the calculation is able to describe the absolute intensity spectrum for a crystal and a copper radiator.

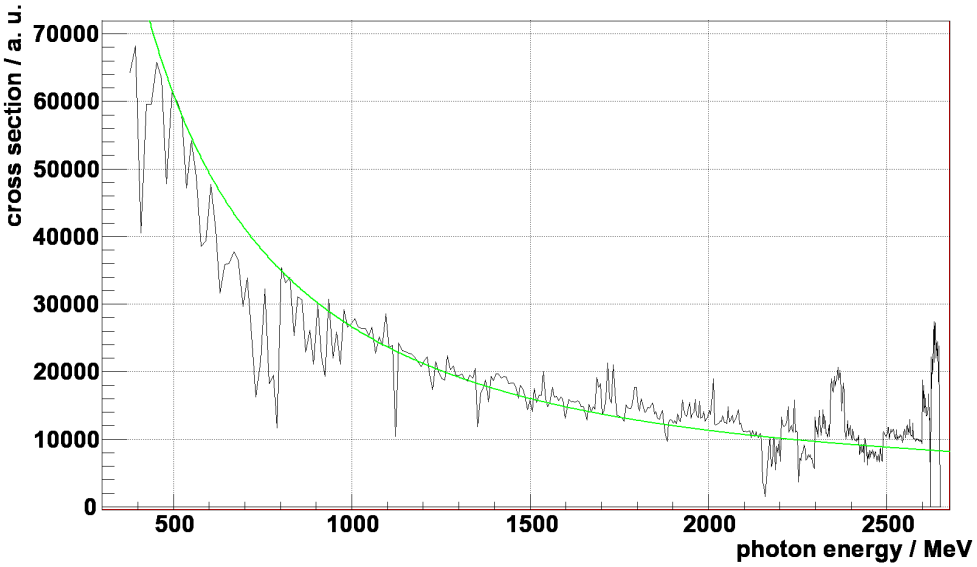

Figure 8.6: Comparision of COBRIS and an uncollimated incoherent intensity contribution from a copper radiator. The measured data is given by the black line, while the green line indicates the simulated incoherent spectrum.

8.3 Comparision of COBRIS with a Collimated Spectrum

In chapter 6 it was explained that the collimation of the photon beam leads to an increase of the degree of polarisation. For the verification of the collimator effect the same data set which was shown for the uncollimated case 8.3 was used again.

But now an additional condition on a present signal of the GIM was set in the data analysis.

To calculate the collimated intensity spectrum the same parameters as for the description of the uncollimated spectrum were used and extended by the collimator parameters $r = 2\,\text{mm}$, $L = 3.26\,\text{m}$ and $ł = 24\,\text{cm}$. Figure 8.8 illustrates the comparison of a calculated relative intensity spectrum with the measured collimated relative intensity spectrum. The maximum degree of polarisation in this intensity spectrum is reached at $E_0 \approx 1245\,\text{MeV}$ with 57.8 %. In this case an increase of the degree of polarisation by 8.6% absolute is achieved by using a collimator. A large discrepancy at the region of the discontinuity is visible. As mentioned in section 8.1, the primary electron beam is not stable and the data which is used is summed over approximately two days. If the electron beam moves during taking data over the crystal, the position of the produced photon beam in the collimator changes. It is possible that the photon beam moves over the restriction of the collimator which would lead to lost coherent intensity contributions in the relative intensity spectrum. Another reason could be that the beam spot size is not included yet. Since this are only assumptions, further investigations have to be done.

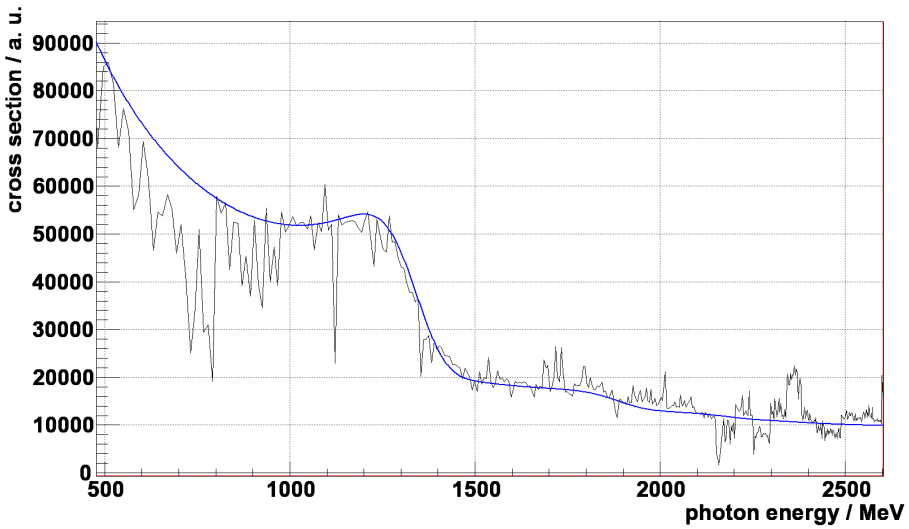

Figure 8.7: Comparision of COBRIS and an uncollimated coherent and incoherent intensity contribution from a diamond crystal. The measured data is given by the black line, while the blue line indicates the simulated coherent spectrum.

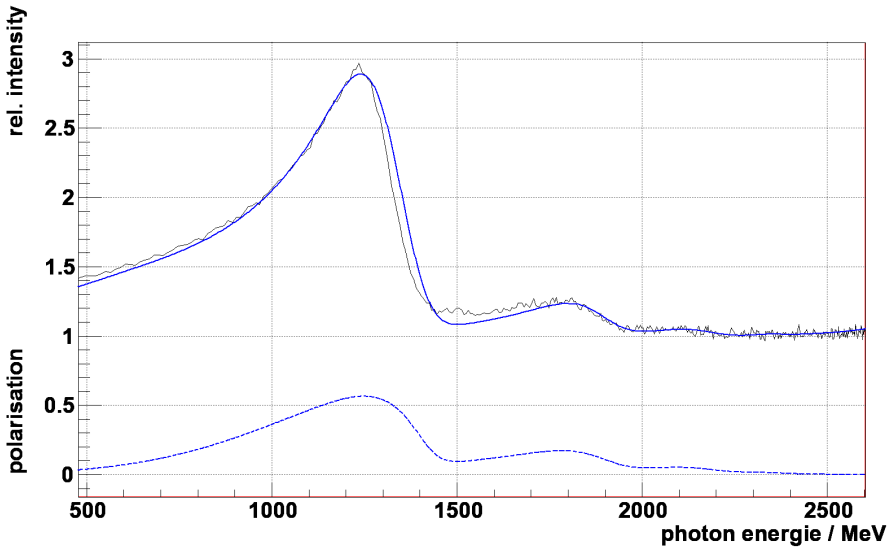

Figure 8.8: Comparision of COBRIS with a collimated relative intensity contribution. The measured data is given by the black line, while the blue line indicates the simulated relative intensity spectrum. The dotted blue line describes the degree of polarisation.

COBRIS is able to describe the coherent intensity contributions in the uncollimated relative intensity spectra. In comparison to the ANB program, the incoherent scaling factor which has to be used to describe relative intensity spectra was reduced to 10%. The consideration of the collimator leads to an increase of the degree of polarisation. Also collimated spectra can be described in a first approximation. It is noticed that variations in the data occur at the coherent edge. This effect is not understanded yet and has to be examined.

9 Summary

The BGO-OD epxeriment which is currently set up at ELSA is designed for the detection of charged and uncharged mesons in photoproduction processes. In order to examine baryon resonances a highly energetic photon beam is required. The production of high energy photons is realised with electron bremsstrahlung. Using linearly polarised photons allows a better seperation of overlapping resonances and improved understanding of the underlying reaction mechanism. To produce linearly polarised photons a crystal instead of an amorphous radiator is used. Because the degree of polarisation depends strongly on the orientation of the crystal with respect to the direction of the primary electron beam, the crystal is aligned precisely by a goniometer.

This diploma thesis has concentrated on the setup of a goniometer system consisting of the goniometer itself, a radiator plate containing amorphous radiators and different tools for the inspection of the primary electron beam and a vacuum tank where the goniometer is placed. Due to severeal malfunctions of the goniometer, it was not possible to implement the goniometer system into the beamline.

In addition, to determine the degree of polarisation a program called COBRIS is written which is mainly based on papers of U.Timm [Tim69], D. Lohman [Loh94] and F.Rambo [Ram98]. COBRIS considers the electron's beam divergence, multiple scattering of the electrons in the diamond and the collimation of the photon beam. For the determination of the degeree of polarisation, the ANB program written by F. A. Natter [Nat03] is currently used at different experiments like CLAS and CB. To describe uncollimated relative intensity spectra adequatly with the ANB program, it is necessary to scale the incoherent intensity distributions by a factor of ≈ 1.5 at CLAS ([Gor04],[Mel05]) and of ≈ 1.35 at CB [Els07] is required. Even though COBRIS also requires a scaling factor with a value of ≈ 1.1. It is now significantly smaller. It is assumed that the requirement of a scaling factor in the incoherent intensity distribution is due to an inadequate description of the form factor.

The consideration of a collimated photon beam leads to an increase of the degree of polarisation. However deviations in the region of the discontinuities are observed. This effect could be explained by the motion of the electron beam over the crystal during data taking. The consideration of the beam spot size is not included yet and could also be a reason for this deviations.

References

[Bet34] BETHE, H.A. The influence of screening on the creation and stopping of electrons. *Phil. Soc.* 30, (1934), S. 524-539

[Boc97] BOCQUET, J. P. et al. GRAAL: a polarized γ-ray beam at ESRF. *Nucl. Phys. A*, 622(1–2):c124–c129, 1997

[Bös11] BÖSE, S. *In preparation.* Dissertation, Universität Bonn, 2011.

[Cre09] CREDE, V. et al. Photoproduction of η and η' mesons off protons. *Phys. Rev. C*, 80(5):055202, Nov 2009

[CW65] Cromer, D.T. ; WABER, J. T. Scattering Factors Computed from Relativistic Dirac-Slater Wave Functions. *Acta. Cryst.* 18, (1965), S. 104

[Dia68] DIAMBRINI, G. High-Energy Bremsstrahlung and Electron Pair Production in Thin Crystals. Rev. Mod. Phys. 40, (1968), S. 611–631

[Eid04] EIDELMAN, S. et al. Review of Particle Physics. *Phys. Lett.* B 592, (2004), S. 1–5

[ELSA] Electronen Strecher Accelerator, Nov. 2010,

[Els07] ELSNER, D. *Untersuchung kleiner Partialwellenbeiträge in der Nähe dominierender Resonanzzustände des Protons mit linear polarisierten Photonen.* Ph.D. thesis, Universität Bonn, 2007 http://www-elsa.physik.uni-bonn.de/Beschleuniger/bilder/elsaplan_en.pdf

[FP09] FORNET-PONSE, K. *Die Photonenmarkierungsanlage für das Crystal-Barrel/TAPS-Experiment an ELSA.* Ph.D. thesis, Universität Bonn, 2009

[Gor04] GORDON, C. I. O. ρ^0 *Photoproduction using Linearly Polarised Photons with the CLAS Detector* Dissertation, University of Glasgow, 2004

[Ham08] HAMMAN, D. *Test und Inbetriebnahme der Prototypdriftkammer für das B1-Spektrometer.* Diploma thesis, Universität Bonn, 2008

[Han11] HANNAPPEL, J. Private communication, 2011

[Hau04] HAUG, E. *The elementary process of Bremsstrahlung.* World Scientific, 2004

[Hig75] HIGHLAND, V. L. Some practical remarks on multiple scattering. *Nucl. Instrum. Methods* 129 (1975), S. 497–499

[Joo96] JOOSTEN, R. *Aufbau und Inbetriebnahme eines hochgranularen Vertexdetektors aus szintillierenden Fasern für das Experiment MOMO an COSY Erste Erebnisse der Reaktion* $p + d \rightarrow {}^3He + \pi^+\pi^-$. Dissertation, Rheinische Universität Bonn, 1996

[LEPS] LEPS Beamline, Sept. 2010, http://www.rcnp.osaka-u.ac.jp/Divisions/np1-b/lepsbl.html

[Live05] LIVINGSTON, K. The stonehenge technique: a new method of crystal alignment for coherent bremsstrahlung experiments. Dabagov, Sultan B. International Conference on Charged and Neutral Particles Channeling Phenomena, Proc. SPIE Bd. 5974, 2005, S. 170–176

[Kit06] KITTEL, C. *Einführung in die Festkörperphysik*, Oldenbourg Wissenschaftsverlag, 2006

[Lan86] LANDAU, L.D ; LIFSCHITZ, E.M. *Lehrbuch der theoretischen Physik, Band 4, Quantenelektrodynamik*, Akademie-Verlag, 1986

[Lau60] VON LAUE, M. *Röntgenstrahlinterferenzen*, Akademische Verlagsgesellschaft., 1960

[Loh94] LOHMAN, D. et al. Linearly polarised photons at MAMI (Mainz). *Nucl. Instrum. Methods* A 343, (1994), S. 494–507

[Mel05] MELONE, J. J. *Measurement of the photon asymmetry fo the* $p(\vec{\gamma}, K^+)\Lambda^0$ *reaction at CLAS from 1.6 to 2.0 GeV* Dissertation, University of Glasgow, 2005

[Mes11] MESSI, F. *In progress.* Ph.D. thesis, Universität Bonn, 2011

[MFO92] MASLEN, E.N. ; FOX, A.C. ; O'KEEFE, M.A. ; WILSON, A. J. C. *International Tables for Crystallography.* Bd. C. Kluwer Academic, Dordrecht, 1992

[MGe08] MCGEORGE, J. et al. Upgrade of the Glasgow photon tagging spectrometer for Mainz MAMI-C. *The European Physical Journal A - Hadrons and Nuclei*, 37:129–137, 2008

[Mol48] MOLIÈRE, G. Theorie der Streuung schneller geladener Teilchen II. *Z. Naturforschung* 3a, (1948), S 78-97

[Moe58] MÖßBAUER, R. L. Kernresonanzfluoreszenz von Gammastrahlung in ^{191}Ir. *Z. Physik* A 151, (1958), S. 124–143

[Nat03] NATTER, F. A. et al. Monte Carlo Simulation and Analytical Calculation of Coherent Bremsstrahlung and its Polarisation. *Nucl. Instrum. Methods* B 211, (2003), S. 465–486

[New] http://www.newport.com

[New1] http://search.newport.com/?q=*&x2=sku&q2=UTS150PP

[New2] http://search.newport.com/?q=*&x2=sku&q2=XPS-C8

[Ram98] RAMBO, F. et al. Enhancement of the linear polarization of coherent bremsstrahlung by collimation of the photon beam. *Phys. Rev.* C 58, (1998), S. 489–501

[Ram07] RAMSEGER, A. *Vorbereitung und Test des Flugzeitdetektors für das Crystal-Barrel-Experiment an ELSA.* Diploma thesis Universität Bonn, 2007

[Sch51] SCHIFF, L.I. Energy-Angle Distribution of Thin Target Bremsstrahlung. *Phys. Rev.* 83 2, (1951), S. 252-253

[Sch95] Schmidt, A. *Aufbau und Inbetriebnahme einer Apparatur zur Erzeugung linear polarisierter Photonen.* Diploma thesis, Insitute of Nuclear Physics, Universität Mainz, 1995

[Sch10] SCHWAN, T. *Test und Inbetriebnahme der Driftkammern für das BGO-OD-Spektrometer.* Diploma thesis, Universität Bonn, 2010

[Sie10] SIEBKE, G. *Design of the BGO-OD Tagging System and Test of a Detector Prototype*, Diploma thesis, University Bonn, 2010

[Tim69] TIMM, U. Coherent Bremsstrahlung of Electrons in Crystals. *Fortschritte der Physik .* 17, (1969), S. 765-808

[Wa] WALTHER, D. et al. technichal drawings

[WL39] WHEELER, J.A. ; LAMB, W.E. *Phys. Rev.* 55, (1939), S. 858

Appendix

A.1 System of Units

The natural unit system is used in this diploma thesis, which is definded by

$$\hbar = c == m_e = 1. \tag{A.1}$$

Due to this definition different physical units getting the same dimension:

$$[\text{mass}] = [\text{energy}] = [\text{momentum}] = [\text{length}]^{-1} = [\text{time}]^{-1} \tag{A.2}$$

Si units are recovered by multiplying

$$\text{length by } \lambda = \frac{\hbar}{m_e c} = 3.8616 \cdot 10^{-13}\,\text{m}$$
$$\text{momentum by } m_e c = \frac{0.511\,\text{MeV}}{c} = 2.731 \cdot 10^{-22} \frac{\text{kg} \cdot \text{m}}{\text{s}^2}$$
$$\text{energy by } m_e c^2 = 0.511\,\text{MeV} = 8.1872 \cdot 10^{-14} \frac{\text{kg} \cdot \text{m}^2}{\text{s}^2}$$

The lattice constant is given by

$$a = 3.567 \cdot 10^{-10}\, m = 923.7 \tag{A.3}$$

Cross sections are given in units of $\bar{\sigma}$

$$\bar{\sigma} = Z^2 r^2 \alpha = 0.57947\, Z^2 = Z^2 \alpha^3 \tag{A.4}$$

Danksagung

Ich möchte mich recht herzlich bei allen bedanken, die mich bei meinem Studium unterstützt und zum Gelingen meiner Diplomarbeit beigetragen haben:

Ich bedanke mich bei Prof. Schmieden für die Vergabe dieses interessanten Themas sowie die Möglichkeit gehabt zu haben am BGO-OD Experiment mitzuwirken.

Bei Prof. Dingfelder bedanke ich mich für die Übernahme des Koreferates.

Herrn Dr. Stefan Goertz möchte ich für die Vertretung für Prof. Dingfelder an meinem Diplomkolloquium danken.

Bedanken möchte ich mich bei Herrn Dr. Daniel Elsner für seine Betreuung im letzten Jahr.

Ich bedanke mich bei Dr. Russel Johnstone, Dr. Tom Jude und Dr. Daniel Elsner für das Korrekturlesen meiner Diplomarbeit.

Mein Dank gilt Holger Eberhardt für die hilfreichen Diskussionen und für die Aufbereitung der Daten dir mir für den Vergleich mit COBRIS zur Verfügung gestellt wurden.

Ein großer Dank gilt der ganzen Arbeitsgruppe für das angenehme Arbeitsklima und den zahlreichen Kuchen.

Zuletzt möchte ich mich für die Unterstützung während meines ganzen Studiums bei meiner Familie bedanken .